# Ligne InterFaces

## INTRODUCTION

En 2011, la ligne IF a fonctionné parfaitement, délivrant 342 shifts de 8 heures de faisceau pour 24 expériences au total, laissant aussi la place à du temps pour la recherche propre des équipes locales ou à la mise au point des techniques instrumentales. La production scientifique de 25 publications dont la moitié dans des revues à fort impact démontre l'intérêt de la communauté scientifique pour les 3 instruments de la ligne IF (INS, GMT, microdiffraction).

# 1 Développements techniques

Les développements instrumentaux faits en 2011 s'inscrivent dans la poursuite de projets déjà lancés : UHV-CVD et micro-diffraction.

Un travail très important a été fait sur l'installation de UHV-CVD et nous avons réussi les premières croissances de nano-fils de silicium. Ces premiers tests ont mis en évidence la nécessité d'utiliser des gaz plus réactifs compte tenu des très faibles pressions de travail, du disilane au lieu de silane, et du digermane au lieu de germane. Ces gaz étant très toxiques, nous travaillons encore à ce jour à l'élaboration des dossiers de sécurité,(protocoles d'utilisation, modes opératoires afin d'obtenir l'accord du service de sécurité de l'ESRF). Nous avons bon espoir d'obtenir un accord pour l'utilisation du digermane. En l'absence d'un tel accord, les études de croissances de nano-fils de germanium seraient fortement compromises voire arrêtées.

Sur la chambre ultravide, nous avons aussi mis en place un nouvel analyseur cylindrique pour la spectroscopie d'électrons Auger. Monté sur un manipulateur spécifique autorisant de très faibles distances de travail (10mm), on obtient un rapport signal sur bruit de 1000:1 ce qui permet une très bonne caractérisation chimique de la surface des échantillons.

L'installation de micro-diffraction en faisceau blanc attire toujours autant d'équipes aussi bien de la communauté nationale qu'internationale. L'utilisation en standard d'une caméra plus performante en terme de bruit de mesure, de correction des défauts de distorsions et de rapidité de lecture permet d'une part de réduire la durée des expériences, et d'autre part de collecter des données de meilleure qualité. La suite logicielle d'analyse LaueTools développé en interne offre désormais aux utilisateurs des outils fiables et performants de traitements des données de microdiffraction en ligne et hors ligne d'analyse des données, compétitifs du logiciel XMAS préexistant. La production scientifique sur cet instrument ainsi que le nombre de projets déposés soulignent l'utilité d'un tel instrument en Europe et sa fiabilité qui n'est désormais plus à démontrer.

Le nouveau banc de microdiffraction qui vise à obtenir une taille de faisceau de 200x300nm est en cours de réalisation et est prévu d'être validé et opérationnel à partir du mois de Mai 2012 (fin du long arrêt machine de l'ESRF). Les miroirs à courbure fixe ont été qualifiés par le service de métrologie de l'ESRF: ils présentent des erreurs de pente inférieure à 0.2µm et une rugosité de 2Å rms en accord avec les spécifications demandées.

# 2 GMT

Cinq expériences d'utilisateurs externes (correspondant à quatre équipes) ont employé le goniomètre multitechnique cette année. La durée moyenne d'une expérience a été de 18 shifts. Dans le domaine de la catalyse, *A. Bailly, M.C. Saint-Lager et al,* ont validé le perfectionnement de leur nouveau réacteur (volume plus petit de la chambre de caractérisation augmentant la sensibilité aux faibles concentrations en catalyseur). L'équipe a pu suivre *in operando* l'hydrogénation de nanoparticules composées d'or et de palladium en combinant la diffusion centrale aux petits angles en incidence rasante (GISAXS) et la diffraction aux grands angles en incidence rasante (GIXRD). A une échelle un peu plus grande, *J. Eymery et al* ont caractérisé les déformations et les défauts dans des nanofils de nitrures de Gallium présentant une structure coeur-coquille par GIXRD. Ces mesures ont contribué à déterminer les principaux paramètres d'élaboration des nanofils et améliorer significativement le protocole innovant de synthèse (*Chen et al, Appl. Phys. Lett. 2011*). En matière molle, le GISAXS a servi à caractériser l'apparition d'une phase organisée de brins d'ADN dans une structure lamellaire en fonction de la concentration en eau. Cette étude approfondit les résultats déjà obtenus sur cet instrument et publiés dans *E. Andreoli , L. Navailles, F. Nallet et al, Europhys. Lett. (2010)*. Enfin, également dans le domaine de la matière molle, *T. Charitat, J. Daillant, G. Fragneto et al* ont, par des mesures de réflectivité et diffusion hors spéculaire des rayons X, complété la compréhension du potentiel mécanique d'interaction entre membranes de phospholipides . Ces dernières expériences ainsi que celles effectuées par *F. Rieutord et al* sur la structure et la morphologie de l'interface de collage moléculaire direct de deux substrats (Si /Si, Cu/Cu etc.) à forts enjeux technologiques, démontrent tout le profit que l'on peut tirer de la combinaison de cet instrument avec les rayons X durs délivrés par l'ESRF (27keV, 45keV) dans l'étude des interfaces enterrées.

Cette année, l'installation de microdiffraction a accueilli 8 expériences dont notamment 4 menées par des utilisateurs provenant de l'étranger. La durée moyenne d'une expérience est comprise entre 12 et 15 shifts. Bien que celle-ci soit plus réduite que sur le goniomètre, le réglage et l'alignement de toute l'instrumentation nécessite au moins 2 shifts à chaque session planifiée de microdiffraction (au moins 4 sessions par an).

Les domaines d'études concernés sont: la métallurgie par des mesures de déformation sur des matériaux polycristallins (Nitruration d'acier par *P. Goudeau et al,* traction d'éprouvette de Ti par *S. Eve et al*), la mécanique de relaxation de la céramique $UO_2$ du combustible nucléaire sous irradiation (*H. Palancher et al.)*, les matériaux appliqués (matériaux à changement de phase contenu dans les DVDs, *M. Schneider et al)* ) et biologiques (relation entre résistance et distribution d'orientation dans la nacre, *Korsunsky et al* d'oxford UK), la mécanique fondamentale à l'échelle du micron d'une part par le suivi *in situ* de l'organisation des dislocations lors du chargement mécanique de piliers de monocristaux de Cu (micro-compression -flexion et -torsion par l'équipe autrichienne de Leoben *C. Kirchlechner, J. Keckes et al*) et d'autre part de la confrontation expérience-modèle de la déformation élastique en fonction de la distance à un joint de macles (*O. Robach, O Castelnau et al*). Enfin, une expérience a été menée en collaboration avec *H. Palancher et al* pour mettre au point et développer la méthode dite “du fil” (permettant de déterminer l'origine du signal de diffraction en profondeur).

## *2.1 Développements techniques et projets:*

### *2.1.1 Nouvelle technique combinant la diffraction Laue et la mesure d'énergie des tâches de Laue au moyen d'un détecteur résolu en énergie (energy dispersive method)*

O. Robach, J.-S. Micha, O Ulrich
*CEA-Grenoble/INAC, 17 rue des Martyrs, F-38054 Grenoble Cedex*

Cette nouvelle méthode expérimentale présente l'avantage de mesurer au même point de l'échantillon pratiquement simultanément le diagramme de diffraction Laue composé de tâches et l'énergie d'une ou plusieurs d'entre elles (laps de l'ordre de la minute). La fiabilité de la détermination du tenseur complet des déformations élastiques (exprimant les distorsions angulaires de la maille et sa dilatation isotrope) par microdiffraction Laue est alors notablement améliorée.

Les performances de deux méthodes de mesure de l'énergie des photons associée aux pics de diffraction ont été comparées et les résultats publiés cette année dans *Robach et al. J. Appl. Cryst. (2011)*: la méthode habituelle utilisant un faisceau rendu monochromatique au préalable (insertion du monochromateur de ligne sur BM32 comme sur les quelques autres lignes équivalentes dans le monde), et la nouvelle méthode conservant l'illumination de l'échantillon par un faisceau polychromatique et analysant en énergie les pics de diffraction avec un détecteur ponctuel résolu en énergie.

L'étude a fait ressortir deux résultats importants :

1) que les deux techniques ont des performances comparables, précision relative de $\pm$ 0.4 $10^{-4}$ sur le paramètre de maille pour un monocristal de Ge non déformé et de $\pm$ 1.3 $10^{-4}$ pour un grain de 1 micron d'UO2 polycristallin très faiblement déformé. La précision est pour l'instant limitée non pas par l'incertitude de la mesure de l'énergie d'une tâche de diffraction, mais par l'incertitude sur la valeur de référence (à dilatation nulle) de l'énergie déduite de l'analyse du diagramme de Laue.

2) qu'il faut tenir compte d'une éventuelle variation de l'orientation du faisceau incident au cours du temps dans la méthode habituelle recommandant ainsi de calibrer fréquemment la position du détecteur par rapport à l'échantillon (et au faisceau incident).

Ce travail, à l'aide des outils logiciels d'acquisition et d'analyses de données développés, ouvre des perspectives importantes de gain de productivité de l'instrument et de fiabilité des mesures.

### *2.1.2 Analyse des données – Développement logiciel de la suite LaueTools*

J.-S. Micha, O. Robach
*CEA-Grenoble/INAC, 17 rue des Martyrs, F-38054 Grenoble Cedex*

Des progrès dans l'automatisation de l'analyse ont été réalisés:

- Recherche de pics sur une série d'images,
- Indexation et raffinement de la déformation sur plusieurs grains trouvés sur une image,
- Indexation et raffinement de la déformation sur plusieurs grains par image sur une série d'image

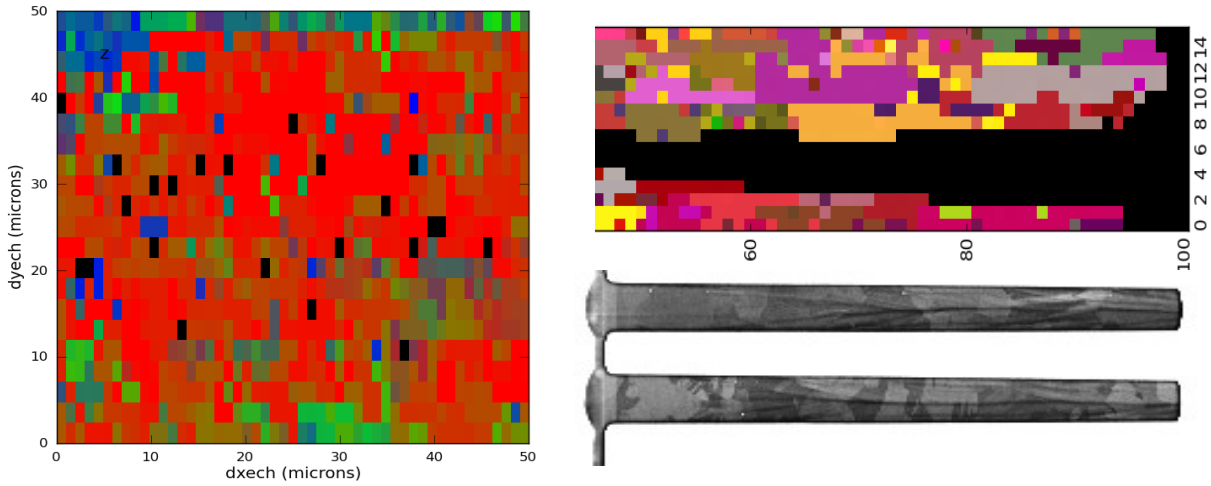


*Figure 1 : Cartographie d'orientation (pas de 1µm) analysée par LaueTools dans le cas (à gauche) d'un polycristal texturé de tungstène (taille de grain ~ 1 µm), et (à droite) sur un « through-silicon-via hemi-cylindre de Cuivre (cliché MEB correspondant) découpé par faisceau d'ions (FIB).*

Un module contenant des tests de références permet de contrôler (et garantir) l'opérationnalité de certains modules de la suite à chaque révision. Des scripts accompagnés des données préalablement analysées constituent une base disponible d'exemples et de tutoriels.

En cours d'expérience, un module permet, à partir de l'analyse du diagramme sur la caméra, de prévoir pour un certain grain la position et l'énergie des spots à mesurer avec le détecteur résolu en énergie placé sur le côté. Après les expériences, il permet en outre l'analyse précise des spectres en énergie provenant du détecteur ponctuel et de traiter la calibration de la relation canal-énergie et deux corrections (décalage lié à l'intensité et la non-linéarité de la relation canal-énergie). Il fournit enfin la dilatation en combinant les résultats de l'analyse du diagramme de Laue (énergie "zéro dilatation") et ceux des mesures d'énergie d'un ou plusieurs spots.

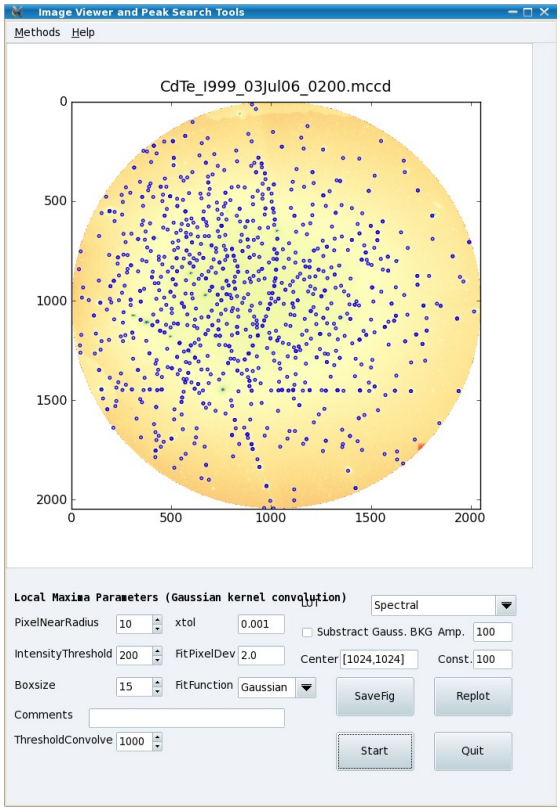


*Figure: Capture d'écran de l'interface graphique du module de recherche et ajsutement de pics de LaueTools.*

## Perspectives

La période d'arrêt de l'ESRF devrait permettre de travailler sur l'automatisation de l'acquisition des données et de leurs traitements à partir de la station centrale de travail (qui contrôle et commande les moteurs et les détecteurs), pour les mesures nécessitant une indexation préalable des diagrammes (ex : méthode de mesure

d'énergie avec un détecteur solide résolu en énergie) et plus généralement pour l'analyse en ligne.

Une interface graphique résumant et affichant les résultats des cartographies (série d'images) est en cours de développement. L'inclusion des stratégies d'indexation "améliorées" (ex : Image Matching) dans l'indexation en série reste aussi à mettre en place.

Dans le cadre du projet ANR AMOS, un budget de 30 K€ a été prévu pour améliorer les performances de la chaine de comptage du détecteur de fluorescence résolu en énergie. La fiabilité, la stabilité et la rapidité de lecture peuvent être sensiblement améliorées. Des tests comparatifs avec un autre détecteur du même modèle ont été ainsi menés par l'équipe du Detector Pool de l'ESRF. Ils mettent en évidence la nécessité de remplacer ou modifier notre détecteur actuel.

### *2.1.3 ANR microstress (début : janvier 2012, durée 4 ans)*

Partenaires: O. Castelnau[1] (coord.), O. Robach[2], C. Maurice[3], L. Saintoyant[4], E. Heripre[5], M. Bornert[6]

*[1] Arts et Métiers-ParisTech/UMR PIMM 8006, 151 Bd de l'Hôpital, F-75013 Paris*
*[2] CEA-Grenoble/INAC, 17 rue des Martyrs, F-38054 Grenoble Cedex*
*[3] Mines St-Etienne/SMS/LCG UMR 5146, 158, cours Fauriel - 42023 St-Étienne Cedex 2*
*[4] EDF R&D/MAI av. des Renardières - Ecuelles 77818 Moret s/Loing Cedex*
*[5] Lab. de Mécanique des Solides, École Polytechnique, F-91128 Palaiseau Cedex*
*[6] Ecole des Ponts ParisTech/Lab. Navier, 6/8 av. Blaise Pascal Champs s/Marne 77455 Marne la Vallée Cedex 2*

**objectif: améliorer de manière signicative la précision sur les déformations intragranulaires.**

L'équipe en charge de la microdiffraction débute une ANR visant à partager et améliorer les savoirs sur la méthode numérique de corrélation d'images (DIC: digital image correlation) appliquée à plusieurs techniques de caractérisation. Cette ANR représente l'opportunité d'implémenter un outil additionnel d'analyse et de traitement des images de microdiffraction.

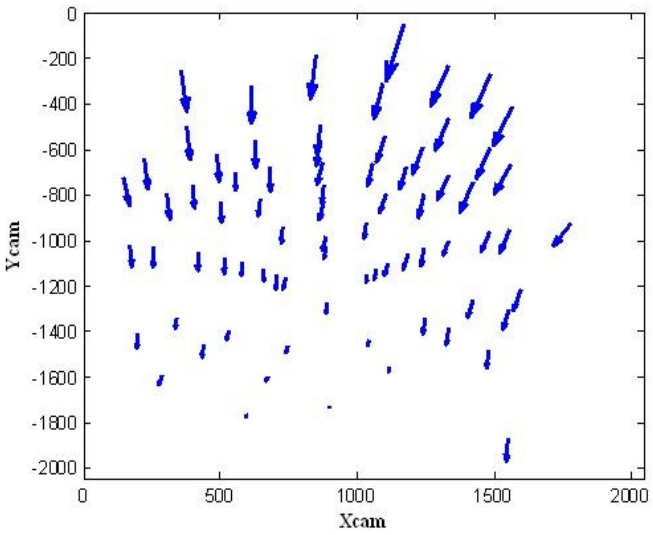


*Figure 1 : déplacement des spots de Laue (x100) entre la fibre neutre et une fibre proche de la surface (dx = 0.9 mm) de la plaque de silicium, obtenue par DIC, pour un chargement de 50 N en flexion 4-points. (réf. J. Petit)*

En microdiffraction Laue, le réseau cristallin peut être utilisé comme "capteur de contrainte locale". Cet aspect intéresse les physiciens de la mécanique et de la plasticité pour relier les mesures du "champ de déformation plastique" et du "champ de contrainte élastique" dans des polycristaux. Actuellement, une précision de l'ordre de $10^{-4}$ peut être obtenue sur les déformations de la maille, mais seulement pour des grains relativement parfaits. Dans la géométrie usuelle de la microdiffraction Laue effectuée sur

BM32 (1 mrad par pixel de caméra), une précision de localisation des spots de diffraction de ±0.1 pixel est alors requise. Cette restriction exige par conséquent des spots de diffraction circulaires correspondant à une faible distribution des paramètres de maille sur tout le volume sondé par le faisceau (pénétration de plusieurs microns).

Il est souhaitable d'étendre le domaine d'application des mesures précises de déformation à des cristaux moins bien cristallisés (plus de défauts comme par exemple un arrangement de dislocations) ou dont la distribution d'orientation ou/et de déformation est plus grande, à l'issue de déformations plastiques de plusieurs pourcents, lors de l'élaboration du matériau ou pendant un test mécanique. Il manque particulièrement une technique de caractérisation X capable de jauger localement la contrainte, dans un cas où le réseau présente un gradient d'orientation significatif sur le volume d'analyse: ce gradient peut comporter une composante lente (rotation progressive provoquant un étalement des spots) mais aussi une composante rapide (sous-joint de grain dédoublant les spots).

O. Castelnau et al.ont posé les bases (réf. J. Petit) de l'utilisation de la DIC à la microdiffraction Laue "Laue-DIC". Cette méthode qui compare les variations de l'intensité diffractée à 2D d'un même spot d'une image à l'autre permet d'augmenter notablement la précision sur la détermination de la variation du tenseur déviatorique des déformations d'un point de l'échantillon à l'autre (ou d'un même grain d'un état de chargement mécanique à l'autre), sans passer par l'inversion directe (source d'erreurs) absolue du diagramme de Laue vers le tenseur. Cette méthode différentielle reposant sur la détection de petits déplacements des spots par corrélation d'images sur des parties du diagramme de Laue, permet de mesurer les variations de la "matrice d'orientation déformée", *M*.

Les étapes prévues dans le projet ANR Microstress correspondent à des applications de la DIC à des cas de complexité croissante : 1) variations spatiales intra-grain de M (grain bien cristallisé puis grain avec fort gradient d'orientation), 2) variations de *M* entre deux états mécaniques du polycristal, en un point matériel donné (*i.e.* un volume d'analyse donné) lors d'une déformation élastique et lors d'une déformation plastique (avec changement de forme des spots).

Dans le premier cas, la méthode Laue-DIC sera combinée avec la méthode dite “du fil” (DAXM: *Differential Aperture X-ray Microscopy*) pour la mesure de variations de *M* le long du faisceau. En effet, le volume de matière sondée ayant une forme allongée dans la direction du faisceau incident, la largeur des spots est comparativement beaucoup plus sensible à la composante du gradient d'orientation le long du faisceau, qu'aux composantes transversales.

Le deuxième cas requiert sur le plan technique un bon contrôle de la position relative du détecteur par rapport à l'échantillon, pour s'affranchir des variations de la position des spots liées au réalignement entre deux étapes de chargements mécaniques.

**Équipement et ressources:**

Un budget de 25 k€ a été ainsi prévu dans le projet ANR Microstress pour motoriser la translation du détecteur. De plus, lorsque les essais mécaniques *in situ* impliquent des déformations plastiques élevées et un champ de déformation fortement non uniforme, un suivi du déplacement des "points matériels" est nécessaire.

De manière complémentaire, un système de DIC optique de mesure du champ de déplacement en surface des échantillons équipera l'installation de microdiffraction (en collaboration avec M. Bornert et financé (30 k€) par le le laboratoire partenaire ENSAM/ PIMM) à l'instar de plusieurs lignes de lumière synchrotron aux USA.
Enfin, le budget de l'ANR comporte un contrat d'un an de postdoc (basé au CEA) pour contribuer au développements techniques associés au projet.

### *2.1.4 ANR Mécanix (début : octobre 2011)*

partenaires:

*[1]IM2NP, UMR CNRS 6242 Faculté des Sciences et Techniques, Av. Escadrille Normandie-Niemen - Case 142 - 13397 Marseille Cedex 20*
*[2] SIMaP 1130 rue de la Piscine - BP 75 - F-38402 St Martin d'Hères Cedex*
*[3] CEA-INAC, 17 rue des Martyrs, F-38054 Grenoble Cedex*
*[4] ID01 beamline ESRF, 6 rue J. Horowitz BP 220 F-38043 Grenoble Cedex 9*
*[5] LPS UMR 8502 Bât. 510 - F-91405 Orsay Cedex*
*[6] MPI Institut für Intelligente Systeme, Heisenbergstr. 3 D-70569 Stuttgart*

Ce projet est coordonné par O. Thomas (IM2NP, Marseille) et implique la ligne ID01 de l'ESRF et le CEA-INAC / SP2M. Il vise à développer une machine pour effectuer des tests mécaniques sur des micro et nano-objets. Cette machine sera conçue pour permettre un suivi précis *in situ* (pendant le test) de la position du micro / nano -objet lors d'expériences de diffraction cohérente (Coherent Diffraction Imaging sur ID01) ou de microdiffraction Laue (sur BM32). En effet, à ces petites échelles et pour ce type d'expériences, lorsque l'échantillon bouge par rotation ou sous l'effet d'un chargement mécanique, il devient plus avantageux effectuer le mouvement relatif faisceau / échantillon en déplaçant le faisceau plutôt que l'échantillon: les accélérations appliquées à l'échantillon perturbent voire rendent le test mécanique de fait infructueux.

Les deux hexapodes placés sous chacun des miroirs focalisant (système optique KB) qui devront prochainement être installés (dans le cadre de la mise à jour de la microdiffraction en 2012) devraient permettre d'effectuer des petits déplacements de faisceau précis et reproductibles.

### *2.1.5 Mesures dans le cadre du projet ANR AMOS :*

O. Robach[1], J.-S. Micha[1], P. Bleuet[2], P. Gergaud[2], L. Clément[3]

*[1] CEA-INAC, 17 rue des Martyrs, F-38054 Grenoble Cedex*
*[2] CEA-LETI-MINATEC, 17 rue des Martyrs, F-38054 Grenoble Cedex*
*[3] ST-Microelectronics, 850, rue Jean Monnet F-38926 Crolles*

Dans le cadre de la comparaison de plusieurs techniques (micro-Laue, TEM et HR-EBSD) de mesures locales d'orientation et de déformation sur le même échantillon, des cartographies micro-Laue ont été mesurées sur une lame d'épaisseur 200 nm taillée dans un circuit microélectronique comportant un via en cuivre (circuit de connexion à travers le silicium).

Ces mesures sur le cuivre devraient offrir des conditions beaucoup plus favorables en terme d'analyse des contraintes que celles effectuées sur des lignes de cuivre sur substrat silicium : en effet, ici les diagrammes de cuivre ne sont pas perturbés par le diagramme de Laue beaucoup plus intense du silicium sous-jacent.

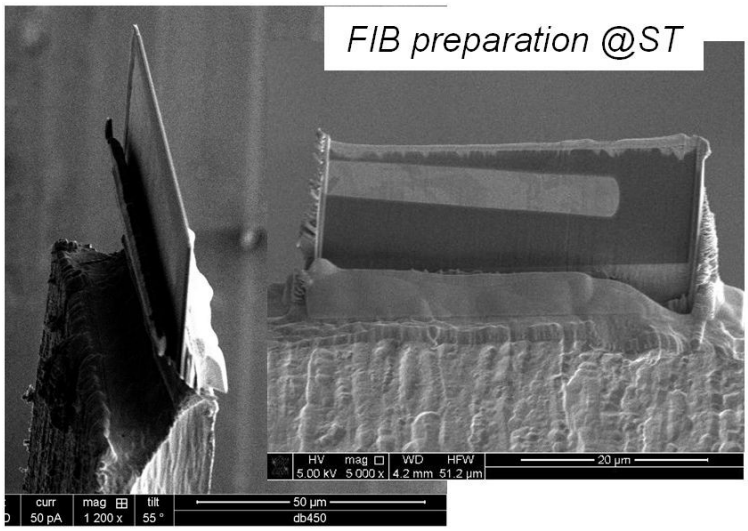


*Fig. 1 : image SEM de la lame TEM découpée au FIB (focussed ion beam) dans un "through silicon via" (TSV) (pilier de cuivre polycristallin obtenu par dépôt électrolytique dans un puits creusé dans du Si monocristallin)*

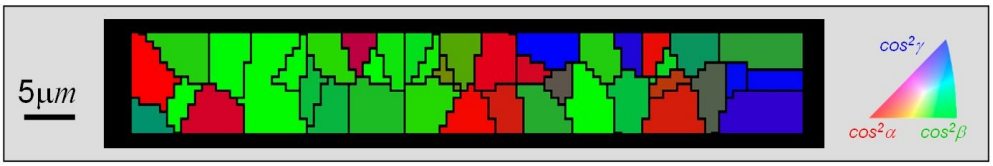


*Fig. 2 : cartographie des orientations dans le via en cuivre. (P. Bleuet, CEA-LETI)*

## 2.2 Sélection de rapports d'expériences

### 2.2.1 Etude de la déformation locale en fonction de la distance à un joints de macles

*O. Robach[1], J. Petit[2], H. Proudhon[3], O. Castelnau[2]*

*[1] CEA-Grenoble/INAC, 17 rue des Martyrs, F-38054 Grenoble Cedex*
*[2] ENSAM/PIMM, 151 Bd de l'Hopital, F-75013 Paris*
*[3] Mines Paris, Paristech/Centre des Matériaux, UMR 7633, BP 87 F-91003 Evry Cedex*

Le but de l'expérience était de cartographier la déformation élastique dans un polycristal comportant de nombreux joints de macle $\Sigma_3$, en fonction de la contrainte appliquée pour voir s'il existe des règles systématiques qui gouvernent l'évolution de la relation d'épitaxie et de déformation entre les deux cristaux, en fonction de la distance au joint les séparant, et en fonction de la contrainte locale.

L'objectif à plus long terme est de trouver des règles qui permettent de résoudre (via une réduction du nombre de paramètres) le problème de l'analyse des contraintes locales

dans les matériaux maclés à l'échelle nanométrique. Pour ces matériaux les diagrammes de Laue sont toujours multi-macles ce qui réduit de façon pathologique le nombre de pics que l'on peut attribuer à un cristallite sans ambiguité.

Pour cette expérience, un matériau à grains très bien cristallisés était nécessaire, afin de favoriser la mesure précise des contraintes. Des cristallites de taille supérieure à 10 µm étaient souhaitables (étant donnée la taille de faisceau de 1 µm) pour des cartographies intra-cristallite.

Deux matériaux ont été utilisés et les données sont en cours d'analyse:

- un superalliage base-Ni "N19" γ/γ' (43% de précipités), avec des grains de l'ordre de 10 µm
- un Monel 400, de composition approximative $Ni_{65}Cu_{35}$, avec des grains de l'ordre de 50 µm.

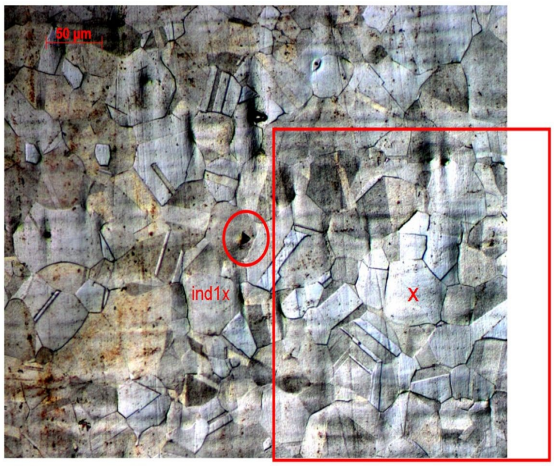


*Fig 1 : image au microscope optique de la surface du Monel, après attaque chimique pour révéler les grains.*

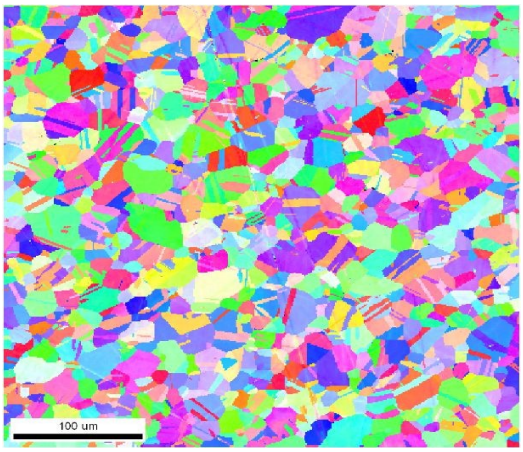


*Fig 2 : Cartographie d'orientation (EBSD) de l'échantillon N19 (F. Adamsky, Mines Paris Tech)*

Le superalliage a l'avantage d'une limite élastique très élevée (1 GPa), ce qui permet des mesures à déformation élastique élevée, plus faciles à réaliser. Le Monel a lui une limite élastique plus faible (mesurée : 75 MPa), mais une cristallinité de surface légèrement meilleure (du fait de l'attaque chimique).

Les essais de traction ont été effectués avec la machine DEBEN de l'ENSAM. Pour l'échantillon N19, une région de 100x100 $\mu m^2$ a été cartographiée avec un pas de 1 µm en x et 2 µm en y, pour 4 étapes de traction : 5 N, 400 N, 800 N et 1200 N. Le dernier point à 1200 N étant légèrement au dessus de la limite élastique. Pour l'échantillon Monel, une région de 250x250 $\mu m^2$ a été cartographié, avec un pas de 2.5 µm en x et 5 µm en y, pour 3 étapes de traction : 5 N, 400 N et 800 N. La limite élastique (vérifiée sur un échantillon provenant du même barreau) correspondant à 1200 N. A l'étape 800 N, la dilatation de la maille a aussi été mesurée avec la méthode basée sur le détecteur résolu en énergie le long d'une ligne traversant deux grains en relation de macle, avec un pas de 1 µm sur plus de 20 µm de part de d'autre du joint.

### 2.2.2 Collage direct de métaux. Etude par réflectométrie X.

F. Rieutord1, F. Baudin2, L. Di Cioccio2

[1] *CEA-INAC, 17 rue des Martyrs, F-38054 Grenoble Cedex*
[2] *CEA-LETI-MINATEC, 17 rue des Martyrs, F-38054 Grenoble Cedex*

Dans le cadre des approches “more than Moore” , l’intégration 3D des circuits est une piste pour augmenter la densité de composants. Le collage direct de métaux, c’est à dire l’adhésion spontanée de deux surfaces à leur mise en contact, suivi d’un recuit limité est une technologie intéressante pour ce type d’approche. Dans ce cadre, nous nous sommes intéressés à l’évolution de l’interface cuivre-cuivre en fonction de la température. D’un point de vue technique, la mesure de l’évolution de l’interface cuivre-cuivre pose un certain nombre de problèmes supplémentaires en comparaison avec les interfaces oxyde de silicium ou silicium. Le cuivre est un matériau dense, fort absorbeur, et les couches observées restent relativement épaisses à l’échelle de la longueur d’onde utilisée. Le signal de l’interface était donc mélangé aux signaux des interfaces Si/TiN et TiN/Cuivre. Malgré ces difficultés, nous avons pu extraire les contributions de l’interface Cu/Cu et tracer les dépendance des largeurs et remplissage d’interface en fonction de la température. Simultanément, nous avons mesuré la déformation du film à partir du suivi des pics de diffraction correspondant à des plans atomiques parallèles et perpendiculaires à l’interface.

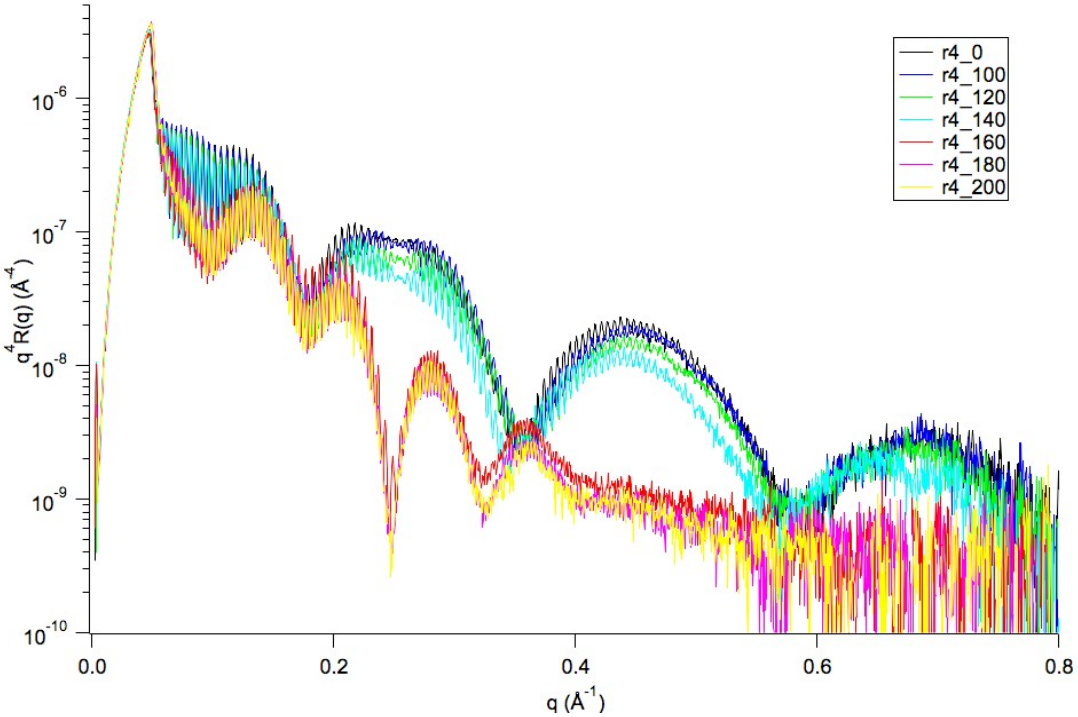


*Figure: évolution de la réflectivité d’interface en fonction de la température. L’interface se ferme aux environ de 200°C ce qui est mis en évidence par la disparition de la composante de Fourier correspondant à une épaisseur de Cuivre.*

### *2.2.3 Effect of the structure of gold-palladium nanoparticles supported on a nanostructured alumina template on their catalytic properties for the butadiene hydrogenation reaction*

Aude Bailly[1], Séverine Le Moal[2], Frédéric Leroy[2], Marie-Claire Saint-Lager[1], O. Robach[3], Georges Sitja[2]

*[1] CNRS - Institut Néel, 25 rue des Martyrs, BP 166, F-38042 Grenoble cedex 9*
*[2] CNRS - CINaM, Campus de Luminy, Case 913, F-13288 Marseille cedex 9*
*[3] CEA-INAC, 17 rue des Martyrs, F-38054 Grenoble Cedex*

The aim of this proposal was to analyze the effect of different Pd compositions on the efficiency of bimetallic gold-palladium nanoparticles (AuPd NPs) during the hydrogenation of 1,3-butadiene. These experiments have been carried out on GMT using the specific equipment developed by the Institut Néel team. By combining GIXRD, GISAXS and mass spectrometry measurements, it allows to correlate the structure and the morphology of model catalysts to their catalytic activity in the course of the reaction. This equipment has been upgraded very recently in order to be more sensitive to the low catalytic activity arising from small amounts of catalyst. Indeed the size of the reactor in which the X-ray and mass spectrometry measurements are performed has been decreased by a factor of 10 (see figure 1). This synchrotron run was the first one using this new configuration; thus enabling us to check whether the equipment matches the requirements. During this experiment, we were able to combine GISAXS, GIXRD and mass spectrometry in order to follow the changes undergone by the catalysts in the course of the hydrogenation reaction. GISAXS patterns, GIXRD scans and mass spectra have been recorded for Pd amounts as low as 0.1 ML; thus confirming the suitability of this experimental set-up for performing such *in operando* measurements with a good sensitivity.

The NPs were grown *in situ* (in the preparation chamber) on a ultrathin nanostructured alumina film obtained by the direct oxidation of a $Ni_3Al(111)$ single crystal. This $Al_2O_3$ film acts as a template promoting the self-organized growth of either mono- (Pd) or bimetallic (AuPd) nanoparticles. By adjusting the respective amount of Pd and Au, the size and the composition of the bimetallic nanoparticles can be independently controlled.
We deposited different thicknesses of pure Pd and pure Au, ranging from 0.1 to 1 ML. We also focused on one specific bimetallic system: 50% Pd-50% Au (0.3 ML in total). In a first step of the experiment and for each system, we checked that the obtained arrays of nanoparticles were effectively very well-ordered. It was evidenced by the GISAXS patterns recorded in UHV, just before exposure to the gases (figure 2, #1).

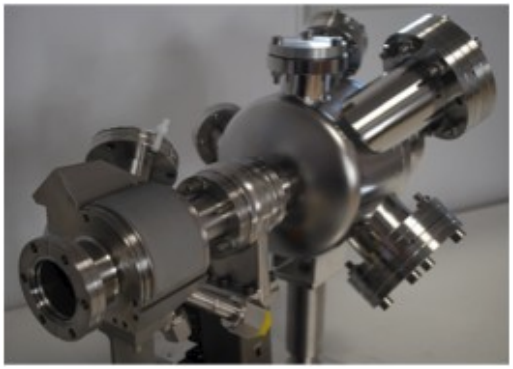

*Figure 1: New reactor for the in operando measurements using X-rays. It is normally coupled to a preparation chamber (not shown here). The X-rays are detected through the large semi-cylindrical beryllium window of the main left-hand side chamber (in which the sample is vertically positioned). The mass spectrometer (not shown) is implanted on the right-hand side chamber; both chambers being connected by a gate valve. The gases are collected in the main chamber and analyzed via a leak valve.*

More surprisingly, the long-range order is preserved under gases, as shown by the GISAXS patterns #2 (recorded in the presence

of hydrogen) and #3 (in the butadiene + hydrogen mixture) of figure 2. This result is of primary importance since the thorough understanding of the catalytic performances implies to be able to quantify the importance of each parameter, i.e. size, shape, crystallographic structure and composition in the case of bimetallic NPs. Thus a disorganization of the NPs array under gases would have precluded any detailed analysis of their catalytic properties.
Additionnally, some slight changes have been observed by X-ray diffraction when hydrogen is introduced. It seems that hydrogen favors one kind of epitaxy relation with respect to the alumina substrate; the detailed analysis being now under progress.

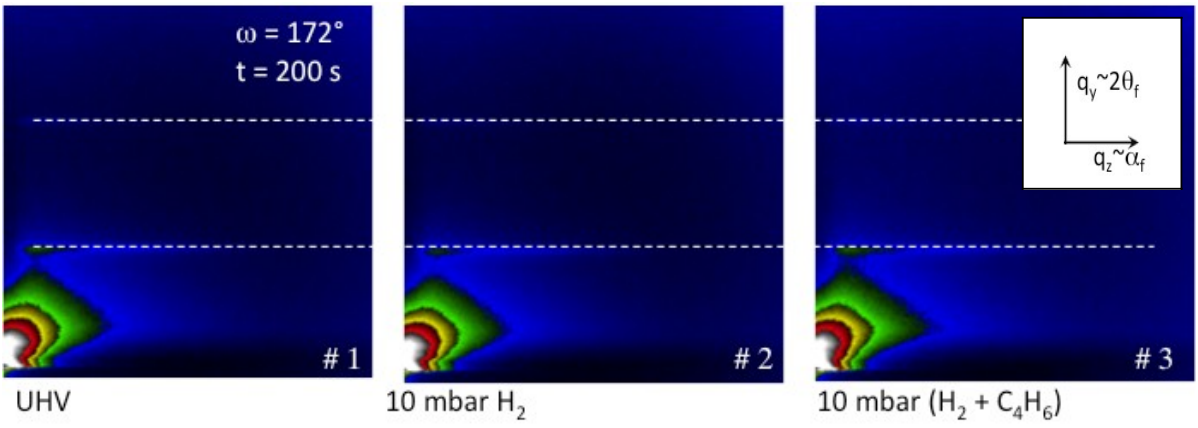


*Figure 2: GISAXS patterns obtained for a 0.3 ML deposit of Pd on a $Al_2O_3/Ni_3Al(111)$ substrate in different environments: #1 in UHV, #2 in 10 mbar of hydrogen and #3 in a mixture of hydrogen and butadiene (ratio 10:1). The white lines indicate the position of the first and second order correlation peaks characteristic of the long-range order of the NPs' array. w and t are the azimuthal angle and the exposure time, respectively.*

Finally, we were able to record mass spectra for catalyst equivalent amounts as small as 0.1 ML in the course of the butadiene hydrogenation. It was also possible to detect differences in the catalytic activity rate of each sample.
Although our results are still mainly qualitative, they indicate that a more detailed analysis, as well as complementary experiments, should make it possible to establish a link between the size, the composition and the catalytic activity of the mono- or bi-metallic nanoparticles.

### *2.2.4 Etude de fils de semiconducteurs de nitrures de Gallium et d'hétérostructures radiales*

J. Eymery[1], R. Koester[1], J. S. Hwang[2], D. Salomon[1,3], X. Chen[1], C. Bougerol[2], J.-P. Barnes[4], D. Le Si Dang[2], L. Rigutti[5], M. Tchernycheva[5], C. Durand[1],6, B. Gayral[1]

*[1] CEA-Grenoble/INAC/SP2M/NPSC 17 av des Martyrs F-38054 Grenoble cedex 9*
*[2] CNRS - Institut Néel, 25 rue des Martyrs, BP 166, F-38042 Grenoble cedex 9*
*[3] CEA-Grenoble/LETI/DOPT 17 av des Martyrs F-38054 Grenoble cedex 9*
*[4] CEA-Grenoble/LETI-Minatec 17 av des Martyrs F-38054 Grenoble cedex 9*
*[5] IEF UMR 8622 - Bât. 220 - Centre Scientifique d'Orsay rue A. Ampère - F 91405 Orsay cedex*
*[6] Université Joseph Fourier, BP 53 38041 Grenoble cedex 9*

Des hétérostructures de nanofils cœur/coquille crûes par MOVPE sur saphir (figure de gauche) ont été étudiées par rayonnement synchrotron et par plusieurs autres techniques (microscopie électronique, nano-SIMS, photo- et cathodo luminescence) [1].

L'objectif principal était de relier les propriétés structurales, en particulier les épaisseurs et les compositions aux propriétés optiques des puits croissants sur les côtés des fils (plans cristallographiques appelés m). L'étalonnage des plans de fils avec des croissances planaires effectué en combinant les techniques de rayons X, de microscopie et de nano-SIMS a permis de comprendre le rôle des épaisseurs (confinement quantique) et de l'absence de champ piézoélectrique dans ces hétérostructures sur leurs propriétés d'émission.

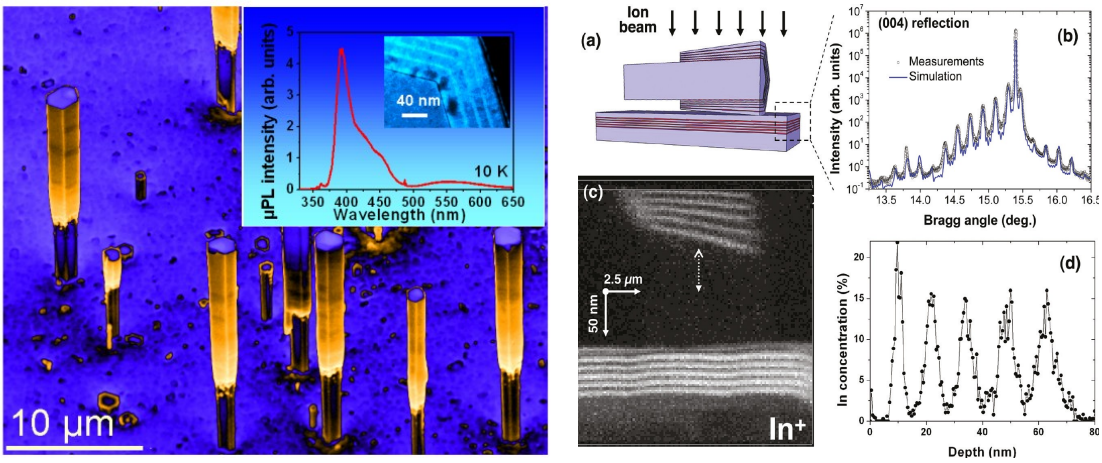


*Gauche : exemple de croissance MOVPE de multipuits quantiques InGaN/GaN sur les flancs de fils de GaN. L'insert montre les propriétés d'émission et une image de microscopie des puits. Droite : cartographie 3D en ion In dans les puits des fils ainsi que sur une référence plane dont les propriétés ont été mesurées sur BM32.*

L'épitaxie de ces hétérostructures a été aussi étudiée sur des substrats de Si ce qui ouvre la voie à leur développement pour réaliser des diodes électroluminescentes.

Des études de diffraction en incidence rasante sur BM32 nous ont également permis d'optimiser les propriétés optiques de fils de plus petits diamètres en validant une méthode originale de faible flux des phases gazeuses [2]. Pour la première fois des propriétés équivalentes aux techniques de MBE ont été obtenues. Ces fils pourront ensuite être utilisés pour réaliser des insertions plus petites de type boîte quantiques.

*[1] M-plane core-shell InGaN/GaN multiple-quantum-well on GaN wires for electroluminescent device. R. Koester, J. S. Hwang, D. Salomon, X. Chen, C. Bougerol, J.-P. Barnes, D. Le Si Dang, L. Rigutti, M. Tchernycheva, C. Durand and J. Eymery, Nano Letters 11 (2011) 4839-4845.*
*[2] Growth of ultra-high quality GaN nanowires by catalyst-free MOVPE X.J. Chen, B. Gayral, C. Bougerol, C. Durand and J. Eymery, Accepted Appl. Phys. Lett.*

### 2.2.5 *From metastable to stable modifications – in situ Laue diffraction investigation of diffusion processes during the phase transitions of $(GeTe)_nSb_2Te_3$ (6 < n < 15) crystals (MA-1194)*

M. N. Schneider[1], X. Biquard[2], C. Stiewe[1], T. Schröder[1], P. Urban[1], O. Oeckler[1]

[1] *Ludwig-Maximilians-Uni./Department Chemie, Butenandtstraße 5 - 13 (Haus D), D-81377 München*
[2] *CEA-INAC, 17 rue des Martyrs, F-38054 Grenoble Cedex*

Micro-focused white-beam (Laue) diffraction using synchrotron radiation is an intriguing method for such investigations. Micro-focusing partially excludes space-averaging effects typical for conventional X-ray diffraction experiments, whereas due to the polychromatic beam large areas of reciprocal space are recorded in a single diffraction pattern. Therefore, micro-focused Laue diffraction is ideally suited for the *in situ* temperature-dependent investigation of diffusion phenomena. Laue diffraction patterns of various GeTe-rich $(GeTe)_nSb_2Te_3$ crystals grown by chemical transport reactions were collected at BM32 (ESRF, Grenoble) using a micro-beam (focus < 1 x 1 $\mu m^2$) in a temperature range from room temperature to approximately 600 °C and a temperature accurancy of ± 15 °C.

Laue diffraction patterns collected from a crystal of $Ge_{0.65(3)}Sb_{0.22(1)}Te = (GeTe)_6Sb_2Te_3$, which was originally grown in the stability range of the cubic high-temperature phase and subsequently quenched (cF. Fig. 2) show asymmetrically broadened reflections which are interconnected by diffuse streaks. The variation of both the asymmetric broadening as well as the diffuse scattering in diffraction patterns collected at different positions on the sample corresponds to the presence of individual twin domains which are at least as large as the area irradiated by the micro-beam. The broadening of the Bragg reflections is related to the varying metric distortion of individual domains along one of the pseudocubic <111> directions. It is further enhanced due to short-range order. The orientation of the structured diffuse streaks between the Bragg positions continues to the asymmetric broadening and indicates the presence of extended planar defects which are parallel but not equidistant. Upon heating at a rate of 10 °C/min, between 250 and 300 °C the diffuse streaks gradually transform into a series of rather sharp reflections characteristic for a long-periodically ordered layered structure (cf. Fig 2, bottom left). Although the Laue experiment does not allow one to determine the absolute lattice parameters, the reflections observed in zones with variable [illegible] roughly match with a 51*R*-type structure. This is in accordance with the cation/anion ratio of $(GeTe)_6Sb_2Te_3$ which determines the thickness of the rocksalt-type slabs. However, such a structure prediction on the basis of simple rules is limited by non-stoichiometry so that details of the long-periodic structure can not unequivocally be determined. At ~500 °C, the characteristic reflections of the layered structure become weak and at 550° the cubic high-temperature modification is formed. The diffraction pattern above this temperature (Fig. 2, bottom right) can be indexed assuming a c*F* lattice with *a* = 6.00 Å in accordance with lattice parameters reported for such high-temperature modifications. The absence of structured diffuse scattering confirms the random arrangement of the cation defects.

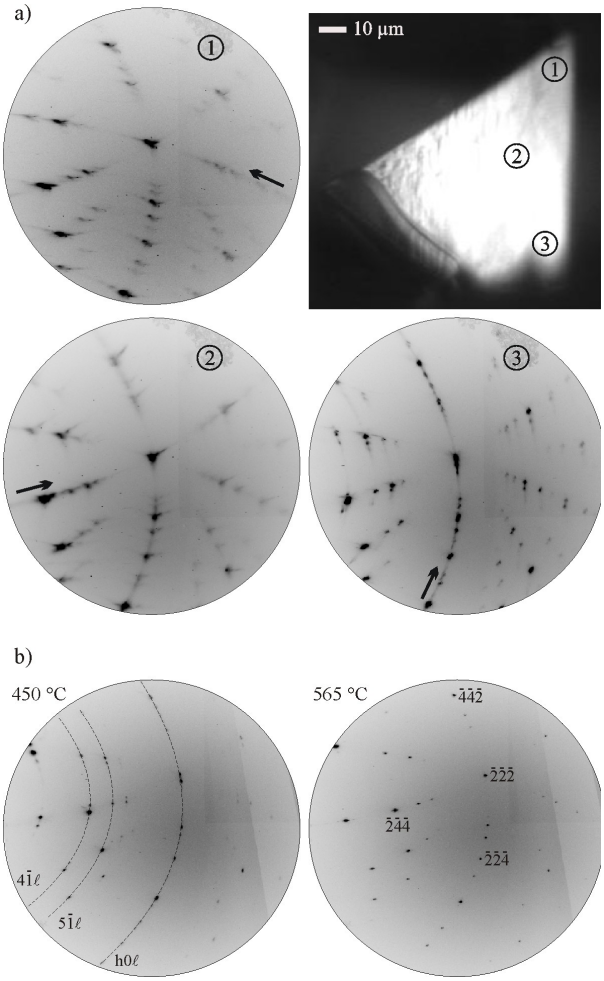


***Fig 2*** *a) Optical microscopy image of the $(GeTe)_6Sb_2Te_3$ crystal used for the investigation (top right) and three room-temperature Laue diffraction patterns collected from the positions indicated by the numbers (black arrows indicate the main orientation of diffuse streaks); b) diffraction patterns collected from position 3 (slightly different section of the complete pattern) at 450 °C (selected rays of the h $\bar{1}\ell$ plane and the h0$\ell$ zone are indicated) and at 565 °C (with selected indices).*

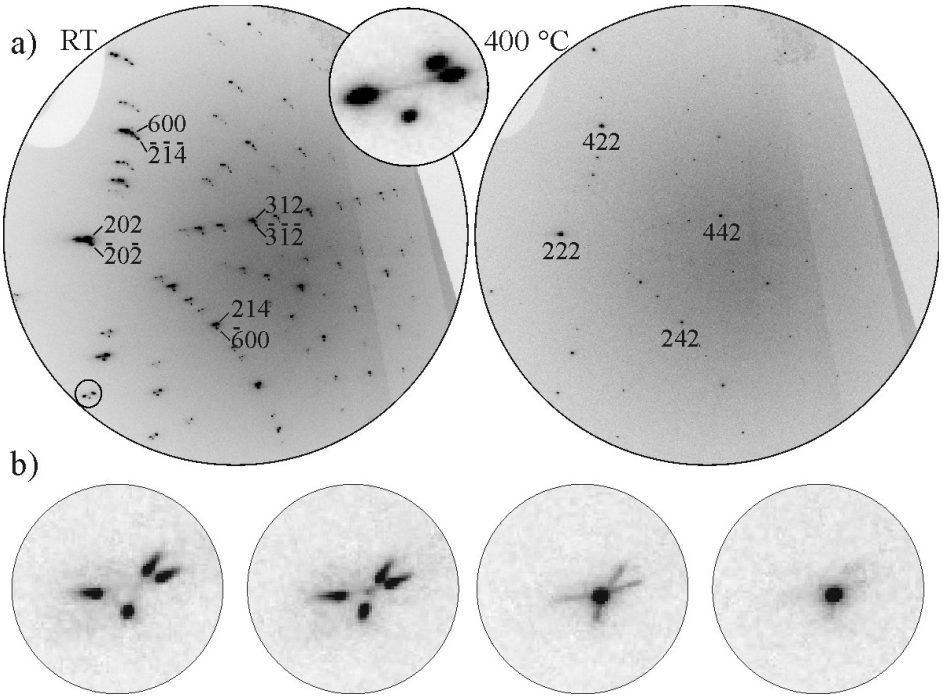


*Fig. 3 a) Laue diffraction patterns of $(GeTe)_{15}Sb_2Te_3$ collected at room temperature and at 415 °C, the inset shows an enlarged group of reflections from different domains (exemplarily indices of some reflections are given); b) changing intensity distribution of the reflection group indicated in a) between 330 and 340 °C (left to right) during heating.*

Laue diffraction patterns of quenched $Ge0.84(1)Sb_{0.12(1)}Te$ = $(GeTe)15Sb2Te_3$ crystals (Fig. 3) do not show strongly broadened Bragg reflections at room temperature, in contrast to samples with lower GeTe content. The diffraction patterns exhibit groups of reflections which result from the superposition of the intensities from individual domains with unit cells clearly deviating from pseudo-cubic metrics. Reflections belonging to individual domains can be indexed based on a h*R* cell with *a* = 4.22 Å and *c* = 10.57 Å. The ratio *a/c* = 0.399 lies between that of α-GeTe (*a/c* = 0.389) and that of a cubic cell in h*R* setting (*a/c* = 0.408). Whereas no diffuse scattering is observed between groups of reflections, there are weak diffuse streaks that interconnect the reflections of one group. These are due to domain-wall scattering (cf. Fig. 3). Upon heating the sample above 330 °C, additional Bragg reflections of the rocksalt-type high temperature phase appear in between the reflections of each group and gain intensity as the rhombohedral distortion of the individual domains decreases. At 400 °C only reflections which can be indexed with a c*F* cell with *a* = 6.00 Å are observed (cf. Fig. 3). In contrast to samples with lower GeTe contents, $(GeTe)_{15}Sb_2Te_3$ does not show nanostructures with pronounced short-range correlated cation defects.

At all temperatures, there was no diffuse scattering indicative of extended planar faults. Intrinsic cation defects can be assumed to concentrate at domain boundaries. However, slightly below the transition temperature to the cubic high-temperature modification, trigonal and cubic domains coexist. Although the $(GeTe)_{15}Sb_2Te_3$ crystal can be viewed as a multiply twinned $Sb_2Te_3$-doped variant of GeTe, the phase transition is different from the continuous, displacive rhombohedral to cubic transition of GeTe at ≈ 432 °C as it requires diffusion of defects from domains boundaries to form the disordered rocksalt type. Upon cooling the crystal below 330 °C, the sharp reflections of the high-temperature

modification significantly broaden and the diffraction patterns resemble to those observed for $(GeTe)_{12}Sb_2Te_3$ at room temperature. This indicates that a nanotwinned transformation twin is formed, whereas before heating a growth twin was present.

### *2.2.6 Strains in light ion implanted polycrystals: influence of grain orientation.*

A. Richard[1,2], H. Palancher[1], E. Castelier[1], J.-S. Micha[3], M. Gamaleri[1], G. Carlot[1], P. Goudeau[2], G. Martin[1], F. Rieutord[3], P. Garcia[1], J.P. Piron[1]

[1] *CEA-Cadarache/DEN/DEC, Centre de Cadarache, F-13108 St Paul lez Durance*
[2] *Institut Pprime, SP2MI, F-86360 Chasseneuil*
[3] *CEA-INAC, 17 rue des Martyrs, F-38054 Grenoble Cedex*

In nuclear materials studies [1,2], light ion implantations offer the prospect of understanding radiation effects in detail or developing new materials with enhanced radiation resistance properties. Indeed ion implantation techniques enable the study of effects resulting from neutron irradiations, without using costly remote handling and characterization facilities.
The primary effect of loading the surface of a material with foreign elements is to generate swelling of the crystal structure. However, the sample is generally not bulk irradiated but exhibits an implanted layer whose thickness typically ranges between a few nanometers and a few microns.
The experiments discussed in the following address the understanding of the relationship between the swelling observed in a bulk (as in nuclear fuels after in-reactor irradiation) and on its surface (ion irradiation case). Characterization of this swelling effect is usually performed using monochromatic high-resolution X-Ray diffraction. However, for polycrystals, it does not enable a comprehensive characterization of the strain field in the surface layer implanted by foreign elements. Moreover, the mechanical models adopted to interpret experiments are usually either simplified (*e.g.* isotropic model) or applied to simplified situations (*e.g.* textured materials) [3,4] which fails to highlight the more general case in which grain orientation has a major contribution. As a consequence both extensive characterization and accurate modelling of the mechanical state of the implanted layer are required.

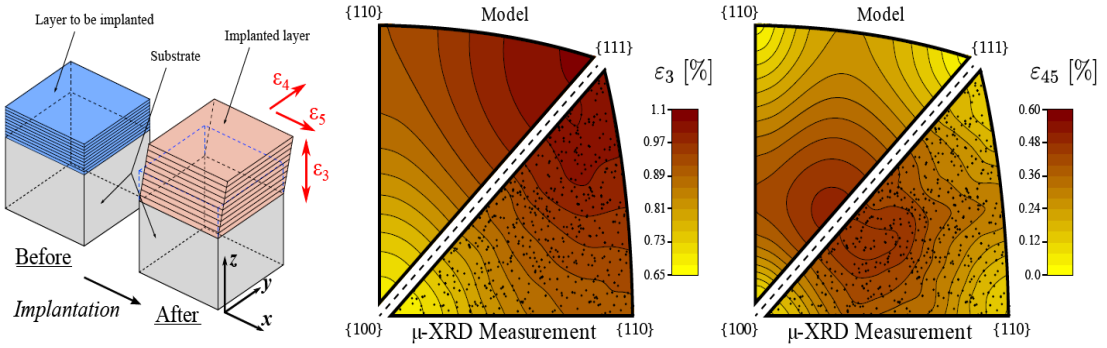


(a) Strain components. (b) Stereographic map of measured and modelled $\varepsilon_3$ (c) Stereographic map of measured and modelled $\varepsilon_{45}$

*Figure 1: Strain originated from He implantation in $UO_2$ polycrystal. a) Schematic of the corresponding grain shape deformation. b and c) Amplitude of strains components as measured with Laue microdiffraction (over several tens of grains) and compared to mechanical model taken into account the $UO_2$ elastic anisotropy.*

On BM32 at the ESRF, it has been measured using µ-XRD in Laue mode that low energy (60 keV) light ion (He) implanted polycrystals exhibit three non zero components of the strain tensor: $\varepsilon_3$, $\varepsilon_4$ and $\varepsilon_5$. Both the normal to the surface ($\varepsilon_3$) and the norm of shear components $\varepsilon_{45}$ amplitudes are highly dependent on the grain orientation. Because experimental data are obtained from the analysis of grains with very different grain orientations, our results rationalize a number of previously reported studies which had failed to recognize the existence of shear components. It is further expected that these components will be modified in the close vicinity of grain boundaries depending on the elastic properties of the interfaces. An elastic mechanical analysis enables us to determine an isotropic swelling strain. This constitutes a first step towards determining, based on surface implantation experiments the extent of radiation induced bulk swelling of irradiated materials.

*[1] B. Radiguet et al, Journal of Nuclear Materials, 104-117 (2010)*
*[2] P. Garcia et al, Nuclear Instruments and Methods B, accepted (2011)*
*[3] U. Laudahn et al, Applied Physics Letters **74** 647 (1999)*
*[4] D. Faurie et al, Applied Physics Letters, **89**, 061911 (2006).*

### *2.2.7 In situ µLaue diffraction on Copper single and bi-crystalline µPillars*

Kirchlechner[1], J. Keckes[1], C. Motz[1], W. Grosinger[1], M.W. Kapp[1], J.-S. Micha[2], O.Ulrich[2], G. Dehm[1]

*[1] Erich Schmid Institute of Materials Science, Montan Univ., Jahnstrasse A-12 8700 Leoben, Austria*
*[2] CEA-INAC, 17 rue des Martyrs, F-38054 Grenoble Cedex*

The deformation behavior of micron- and submicron sized single crystals has intensively been investigated during the last decade. At this small scale, a major difference compared to the macroscopic world is the significantly increased of the flow stress. In the years 2009 and 2010 an *in situ* micro-mechanical test apparatus has been installed at BM32 in order to follow the pioneering approach of Maaß and co-workers [1,2]. The *in situ* indenter is now fully operational and is now used to focus on a new aspect of size dependent plasticity: the behavior of grain and twin boundaries at the micron scale

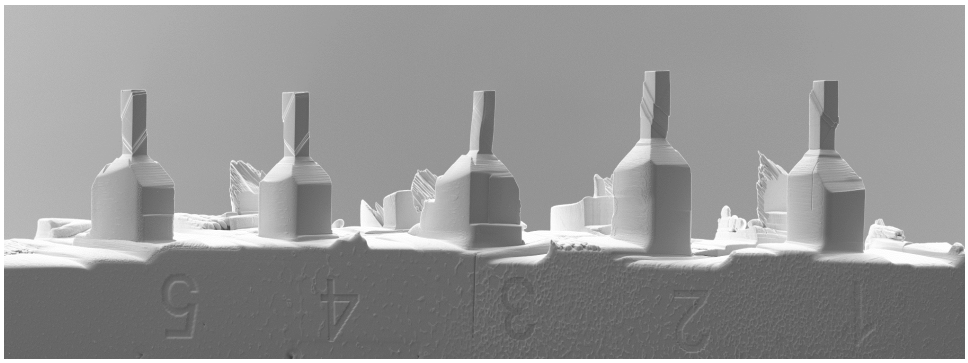


*Fig. 1 SEM micrograph of in situ deformed µPillars made of (5,4) grain A, (3) a bi-crystal consisting of grain A and B and (2,1) grain C (cutting made by FIB).*

Fig. 1 represents a Scanning Electron Microscopy (SEM) picture of five pillars that have been deformed during the *in situ* µLaue experiment. The first two pillars (Fig. 1 indexed 5 and 4) are single crystalline and were cut from grain A whose orientation favors multiple slips activation during compression. The last two pillars (2 and 1) are also single crystalline but cut from grain B, which activates only a single slip. Finally, the middle pillar (3) is a bi-crystalline pillar consisting of grain A and B separated by a grain boundary. The study of the bicrystal is a classical test but performed usually at larger scale.

The first qualitative µLaue results are shown in Fig. 2. In case of the single crystalline pillar (Fig. 2a) the diffraction peaks are just slightly streaked after 20% strain. Only at the sample center Geometrically-Necessary-Dislocations (GNDs) are stored. However, in the bi-crystalline sample, a huge peak streaking and the formation of split Laue spots evidences the storage of GNDs and – in parts – the formation of a dislocation cell structure. Moreover, the observed stress-strain behavior with tremendous hardening for the bi-crystalline sample and minor to no hardening for the single crystalline samples fully agree with this observation.

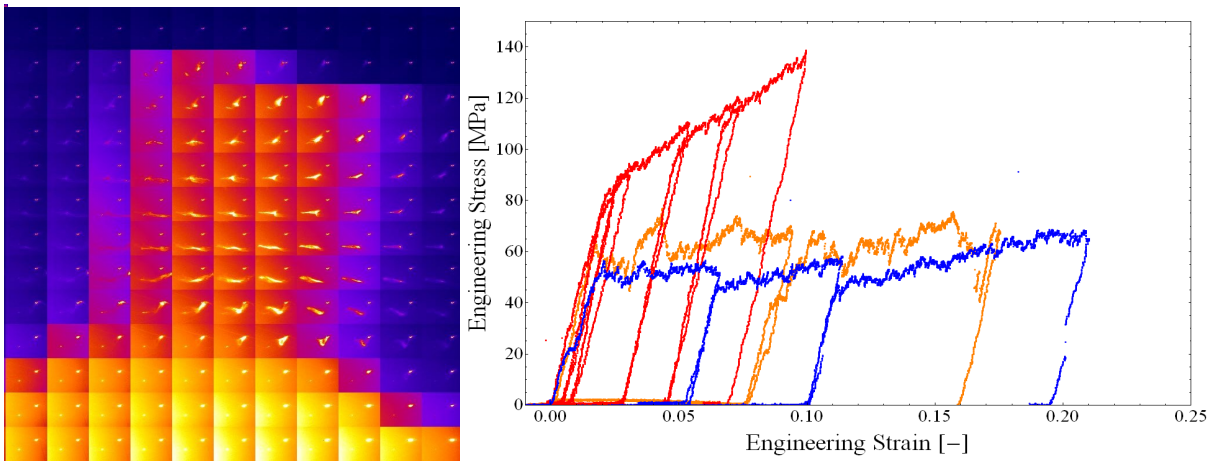


*Fig. 2: (a,b) Composite Laue image showing the same Laue spot as a function of the postion in the pillar of (a) a single crystalline compression sample after 20% strain and (b) a bi-crystal compression sample after 7% strain. Note that the streaking is much more pronounced for the bi-crystalline sample compared to the single crystalline one shown in (a). In addition, the engineering stress versus strain curve is shown (red=bi-crystal, blue = grain A, orange = grain B).*

The implementation of *in situ* test methods for micromechanics at BM32 performed during former beamtimes enables to answer more sophisticated questions in material science, as shown by this experiment. The data evaluation of data obtained during this beamtime is still ongoing, however, the first results qualitatively show the power of µLaue at BM32 to study the behavior of grain and twin boundaries at the micron scale. The quantitatively analyzed data will be used for models describing the dislocation-grain boundary-interaction. Additional beamtime for experiments and one with a possible load sign reversion (fatigue) will be asked in the next selection round.

*[1] Uchic MD, Dimiduk DM, Florando JN, Nix WD. Science, **305**, 986 (2004)*

*[2] Maaß R, Van Petegem S, Van Swygenhoven H, Derlet PM, Volkert CA, Grolimund D. Phys. Rev. Lett., **99** (2007)*

*[3] Kirchlechner C, Keckes J, Micha JS, Dehm G. Advanced Engineering Materials **13**, 837 (2011)*

*[4] Kirchlechner C, Keckes J, Motz C, Grosinger W, Kapp MW, Micha JS, Ulrich O, Dehm G. Acta Materialia, **59**, 5618 (2011)*

### *2.2.8 Osmotic pressure effect on supported bilayer: an off- specular study*

T. Charitat[1]; J. Daillant[2]; A. Hemmerle[1]; G. Fragneto[3]

[1] *Institut Charles Sadron, CNRS - UPR 22, 23 rue du Loess, BP 84047, F-67034 Strasbourg Cedex 2*
[2] *CEA-Saclay/SiS2M/LIONS, UMR 3299, Centre d'Etudes de Saclay Bât. 125, F-91191 Gif-sur-Yvette Cedex and SOLEIL, L'Orme des Merisiers, Saint-Aubin - BP 48, F-91192 Gif-sur-Yvette Cedex*
[3] *Institut Laue-Langevin, BP 156, 6, rue Jules Horowitz F-38042 Grenoble Cedex 9*

Interactions of lipid membranes are not only crucial for membrane fusion and trafficking, endoand exocytosis...[1], they are also fascinating from the physical point of view. Membranes indeed exhibit extremely complex interactions with their environment where molecular scale enthalpic (hydration, van der Waals, electrostatic...[1,2]) and fluctuation related entropic contributions [3] are inextricably involved. Determining the interaction potential between bilayers is challenging and first studies were performed on multilamellar stack where static defects can dramatically affect bilayer interactions. We have recently reported X-ray [4] coupled analysis of specular and off-specular reflectivity leading to a refine caracterization of membrane elastic parameters and interactio potential on Double supported Bilayer (DB).

The aim of the experiment was to measure the elastic parameters of a supported bilayer for water thicknesses comparable to those one can find in multilamellar systems. In order to reach this goal, we applied an osmotic pressure with an hydrosoluble polymer (PVP), to double supported bilayers of DSPC in both gel and fluid phases (Figure 1(a)). We have also investigated the contribution of the electrostatic interaction due to the dissociation charges of our membranes. To do this, we added various concentrations of salt to our systems, and measured the curvature of the interaction potential by a coupled analysis of specular and off-specular reflectivity. Some experimental results are shown on figure 1(a) (insert).

The effects of added polymer (PVP) in bulk solution has been analyzed, and clearly shows that we can apply an osmotic access to a supported DB. As shown on Figure 1(b), our results are in good agreement with theory and compare well to results on multilamellar systems [5]. It opens the way for investigation of small inter bilayer distances were the interaction potential is dominated by the hydration repulsion.

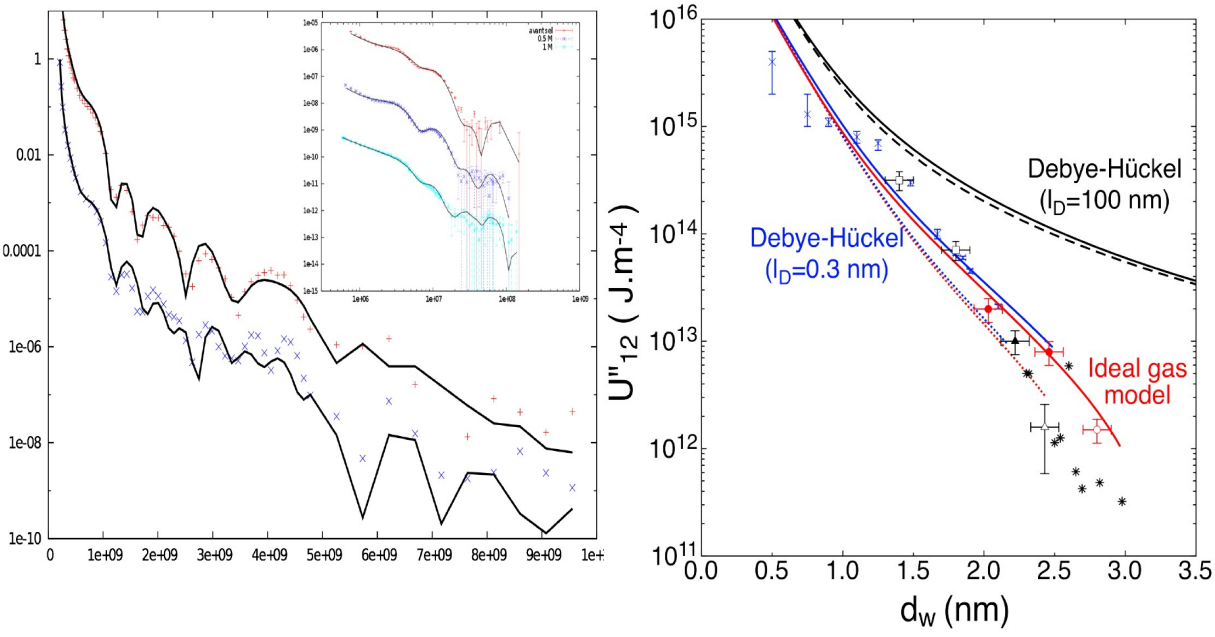

*Figure 1: (left) Upper curve: specular reflectivity of a double bilayer in gel phase and best fit; lower curve : same sample with an osmotic pressure applied. (Insert) Off specular reflectivity of a double bilayer with different concentration of salt in the solvent. (Right) Interaction potential second derivative U" as a function of interbilayer distance dw. (X blue cross) data from Petrache et al [5] for EPC in fluid phase, all other data from this work using DSPC: (O empty red circle) Fluid phase (T=58°C) without added salt; (full red circle) Fluid phase (T=58°C) with added salt (lD=0.7 nm and 0.3 nm); (D) Gel phase (T=40°C) without added salt; (triangle noir) Gel phase (T=40°C) with added salt (lD=0.3 nm); (black square) Gel Phase with applied osmotic pressure. Red solid (respectively dotted) lines were calculated using the soft-confinement potential plus electrostatic contribution described by Ideal Gas model in Fluid (respectively Gel) phase. Blue solid (respectively dotted) lines were calculated using the soft-confinement potential plus electrostatic contribution described by Debye-Hückel model (lD=0.3 nm) in Fluid (respectively Gel) phase. Black solid (respectively dotted) lines were calculated using the soft-confinement potential plus electrostatic contribution described by Debye-Hückel model (lD=100 nm) in Fluid (respectively Gel) phase.*

The experiments with added salt clearly showed that the electrostatic contribution to the interaction potential has to be taken into account. The salt screened the electrostatic interaction and led to smaller thicknesses and higher curvatures of the potential, as predicted by the theory. In figure 1, red solid (respectively dotted) lines were calculated using the soft-confinement potential [6] plus electrostatic contribution described by Ideal Gas model [6] in Fluid (respectively Gel) phase. Blue solid (respectively dotted) lines were calculated using the soft-confinement potential plus electrostatic contribution described by Debye-Hückel model (λD=0.3 nm) [7] in Fluid (respectively Gel) phase. Black solid (respectively dotted) lines were calculated using the softconfinement potential plus electrostatic contribution described by Debye-Hückel model ($\lambda_D$=100 nm) in Fluid (respectively Gel) phase. We are thus sensitive to very small amount of charge surface, and able to describe electrostatic interactions between bilayers for various Debye lengths.

The beamline BM32 was working well and the beamtime was used at 100 %. Sample preparation was also satisfactory, according to both quantitative (transfer rates reproducibility > 95 %) and qualitative criteria.

*[1] Sackmann, E. Physical Basis of Self-Organization and Function of Membranes: Physics of Vesicles, Handbook of Biological Physics, Elsevier Science B.V., 213 (1995).*
*[2] Lipowsky, R., Handbook of Biological Physics, Elsevier Science B.V., 521 (1995).*
*[3] Helfrich, W., Elastic properties of lipid bilayers: theory and possible experiments, Zeitschrift für Naturforschung, **28**, 693 (1973).*
*[4] L. Malaquin, T. Charitat, J. Daillant, Supported bilayers: Combined specular and diffuse X-ray scattering, European Physical Journal E, **31**, 285 (2010).*
*[5] H.I. Petrache, N. Gouliaev, S. Tristram-Nagle, S. Zhang, R.M. Suter, J.F. Nagle, Physical Review E, **57**, 7014 (1998).*

# 3 In situ growth of Nanostructures on Surfaces (INS)

## *3.1 Personnel et développements*

### 3.1.1 Personnel

L'équipe INS est composée d'un chercheur CEA (Gilles Renaud), de deux post-doctorants CEA (Nils Blanc et Valentina Cantelli) d'un chercheur CNRS (Maurizio De Santis) et d'un ingénieur de recherche CNRS (Helio Tolentino).Ils partagent leur activité d'accueil sur l'instrument avec une activité de recherche propre menée sur IF et dans leur laboratoire d'affiliation. Le support technique est assuré par Olivier Geaymond, très actif dans le support des expériences, dans les développements techniques et dans la maintenance, bien qu'il ait aussi en charge aussi le support technique de la partie optique de la ligne. Olivier Ulrich intervient dans le développement de nouveaux projets et dans l'instrumentation (électronique, détection, informatique). Depuis 2007, avec le départ de Marion Noblet-Ducruet, le support technique sur INS est insuffisant. En 2010 un jeune technicien a été embauché en contrat CDD, mais ce poste n'a pas été renouvelé en 2011. L'instrument SUV reste techniquement très complexe et demande un suivi quotidien. Il serait donc hautement souhaitable de remplacer ce départ.

A partir d'octobre 2010, le nouveau système CVD, à très basse pression, est opérationnel sur INS. Ce système utilise les gaz précurseurs pour la croissance des nanofils de silicium et germanium sur différents types de substrats. Cette installation est unique au monde. Elle devrait permettre d'étudier les mécanismes et les phénomènes mis en jeu durant la croissance par CVD, depuis le dépôt du catalyseur métallique (MBE) jusqu'à la formation et l'évolution des nanofils (CVD). Le projet, soutenu par le CEA/INAC et financé par la Fondation Nanoscience, comprend un poste de Post-Doc (Valentina Cantelli), auquel est associé une thèse (Tao Zhou). Plus de détails sur la CVD sont donnés par la suite dans le rapport d'expérience correspondant.

### 3.1.2 Développements

Un nouvel analyseur cylindrique pour la spectroscopie d'électrons Auger (CMA 100 OMICRON Nanotechnologie) a été installé sur la chambre ultravide. Ce détecteur fonctionne en mode analogique ou comptage d'électrons avec une haute transmission et un excellent rapport signal/bruit (1000:1). Il est rapide et facile d'usage. Il répond complètement aux besoins de caractérisations chimiques de la surface pendant les expériences de diffraction X. Un manipulateur (voir figure) conçu par le Service d'Etudes et de Réalisation d'Appareillages Scientifiques (SERAS) du CNRS Alpes permet de s'approcher à la distance de travail (10 mm) et de viser l'échantillon positionné à l'homocentre de la chambre. C'est la clef des performances du nouveau CMA par rapport à l'ancien, qui était lui positionné à 80 mm, une amélioration qui a été rendue possible grâce aussi à l'encombrement réduit de la partie située en ultravide de la nouvelle tête goniométrique, par rapport à celle d'origine.

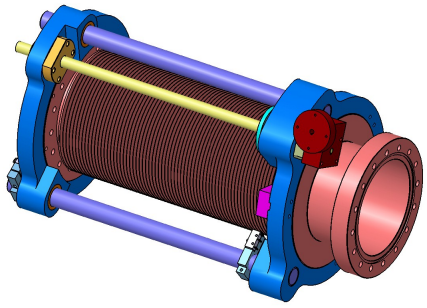

*Schéma du manipulateur du CMA*

## *3.2 Résumés scientifiques INS*

Dans la période comprise entre novembre 2010 et octobre 2011, 12 expériences ont été effectuées sur l'instrument INS (7 attribuées par le comité français, 5 par celui ESRF) avec une durée moyenne de 18 shifts de 8 heures chacune.

### *3.2.1 In-situ* X-ray diffraction studies of the homo-epitaxial growing modes of Ge and Si by Chemical Vapour Deposition on Ge(111) and Si(111) (32-3-699)

V. Cantelli, T. Zhou, O. Ulrich, G. Renaud (CEA Grenoble) ; O. Geaymond (CNRS, Institut Néel)

Nanoscale one-dimensional materials have been stimulating great interest thanks to their unique mechanical[1], thermoelectrical[2], and optical properties relative to their bulk counterparts. NWs are usually grown by chemical vapour deposition (CVD) following the vapour–liquid–solid (VLS) mechanism, first proposed in 1964 for larger (micrometer-scale) 'whiskers'[3], in which NWs spring up from catalyst-substrate eutectic droplets (AuSi - AuGe) under flux of Si / Ge provided by the decomposition of precursor gases. Heterostructures such as Si/Ge NWs are grown by changing the source gas[4]. A catalyst that is in the solid rather than liquid state can also be used, leading to a vapor–solid–solid (VSS) growth mode.

Many aspects of the VLS growth are still not well understood because phenomenological considerations are extracted mainly by *ex situ* investigations, *i. e*. once the VLS process stopped and at RT. Experimental methods that follow growth dynamics and extract quantitative parameters remain a challenge requiring instruments of unique performance. A deep understanding of the crystallographic characteristics and morphology evolution as a function of the growing parameters is an essential step to control the NWs formation. X-ray scattering investigation methods, GISAXS and GIXD, are applicable under gas-atmospheres and can non-destructively probe the structural properties of nanostructures during growth and the evolution of surfaces, providing very valuable information as they average over millions of nanostructures. GISAXS grants access in a statistical manner to the morphological information (size, spacing, and faceting)[5-7] and GIXD provides in addition an unparalleled view on the structural properties such as stress/strain, atomic composition,and defects[7-9]. All these considerations motivated few years ago the launch of a priority program of our laboratory, supported by the Nanoscience Foundation, to develop UHV-CVD capabilities on the existing UHV-INS chamber (In situ Nanostructure growth on Surfaces - operated by CEA and CNRS), with associated Post-Doc and PhD funding. From the end of August 2010, the INS instrument is equipped with UHV-CVD gas injection system for hydride semiconductor gas precursors up to a working pressure $5 \times 10^{-4}$ mbar. The flexibility of this growth system allows working at base pressures of $10^{-11}$-$10^{-10}$ mbar for ultra clean surface preparations, MBE growth of the metal catalyst and a quick change to UHV-CVD conditions avoiding surface contaminations. Figure 1 gives a graphical overview of the installed gas injection system. Ultra pure gas precursors (Silane ($SiH_4$) as Silicon source, pyrophoric installed on August 31st 2010; Disilane ($Si_2H_6$) as Silicon source, pyrophoricinstalled on January 18th 2011 and Germane ($GeH_4$) as Germanium source, highly toxic and pyrophoric installed on January 21st 2011) are injected at very low pressure and flow rate (down to 0.02 sccm), causing a jet of molecules that is well oriented by a quartz guiding cone (final inner diameter: 0.5 mm, length 444 mm) to the sample surface, provoking a local pressure increase without strongly affecting the average pressure in the chamber. In this way, additional analysis tools such as RHEED and Auger electron spectrometry can be used to monitor the CVD process.

Due to the dangerousness of the employed gases, this installation, designed according to the ESRF safety regulations, is equipped of three hydrides detectors, two for ambience and one for the exhaust: a simultaneous alarm of 0.3 ppm of the two hydride open air detectors will cause the evacuation of the whole ESRF experimental hall. Whatever operation with the gas distribution system must be previously approved by the ESRF safety group and at least two authorized operators from the beam-line staff must be present at all time during the experiments. All pressure and flow readouts, as well as gas and heat detectors are connected to a central automated controller that automatically regulates the closing/opening of the valves, the pumps and the exhaust, reducing the human intervention to the operation of the gas mass flow controller.

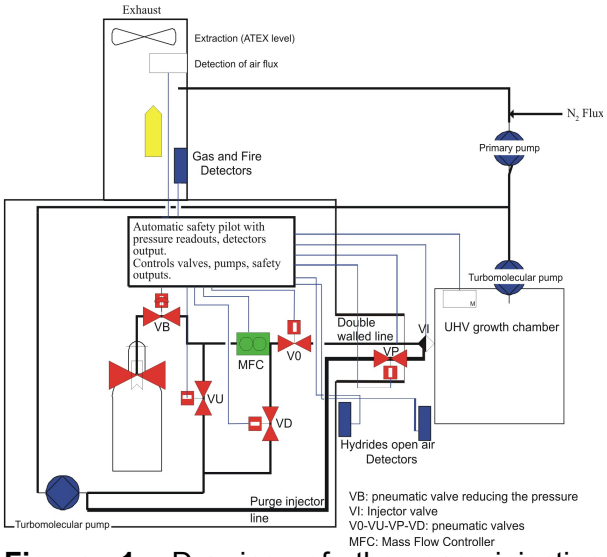


**Figure 1:** Drawing of the gas injection system, representing one gas injection line.

The extension of the existing UHV-MBE system to CVD compatibility offers a promising tool of a unique flexibility for sample growth, which can respond to fundamental questions concerning structural parameters still under discussion in theoretical and applied research.

***Preliminary studies***

The gas sources of Silane and Disilane have been investigated by exploring the Si – Au phase diagram around the eutectic temperature. In the first case Au was deposited by MBE on a sapphire substrate ($Al_2O_3$) in order to prevent the substrate to supply Silicon to the Au droplet. At a constant temperature a long exposition to Silane constant flux of 0.6 sccm allowed to obtain the complete disappearing of the crystalline signal of 50 Å of Au after about 6 hours (figure 2).

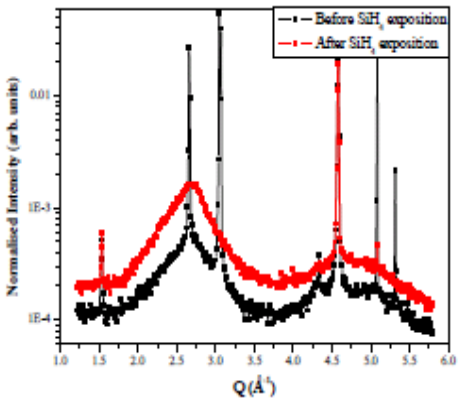


**Figure 2:** Au deposited on sapphire: The Au droplets melt because of exposition to $SiH_4$.

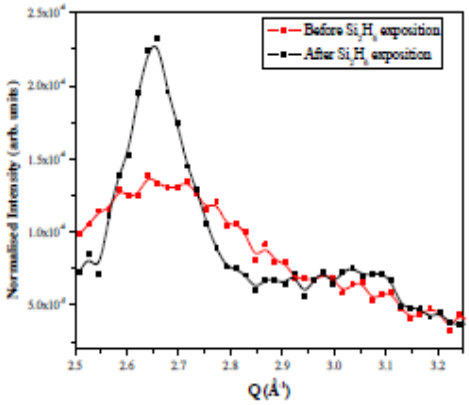


**Figure 3:** Au deposited on sapphire: The Au droplets melt because of exposition to $Si_2H_6$.

For comparison, in figure 3 is reported the fusion of 16 Å of MBE deposited Gold on $SiO_2$ substrate at 370°C as a consequence of 120 s of exposition to the $Si_2H_6$ source at 0.03 sccm.

This experiment clearly evidences the much higher reactivity of Disilane if compared with Silane. Moreover from by successive rapid scan around the (220) Au signal is possible to

monitor the state change of the Au nanoclusters even in a fast regime reaction as with Disilane, usually applied to investigate NW growth at pressure in the order of $10^{-5}$ mbar.

**References :**


[1] W. Q. Han, *et al.,* Science **277** (1997) 1287
[2] L. D. Hicks *et al.*, Phys. Rev. B **47** (1993) 16631
[3] R. S. Wagner *et al.*, Appl. Phys. Lett. **4** (1964) 89
[4] F. M. Ross, Rep. Prog. Phys. **73** (2010) 114501
[5] G. Renaud *et al.* Science **300** (2003) 1416
[6] F. M. Ross *et al.* Phys. Rev. Lett. **95** (2005) 146104
[7] T. David *et al.* Surf. Sci. **602** (2008) 2675V
[8] T. U. Schülli, *et al.*, Nature **464** (2010) 1174
[9] J. Eymery *et al.* Nano Lett. **7** (2007) 2596

### 3.2.2 In situ monitoring of strain relaxation during the deposition of the shell in GaN/$Al_xGa_{1-x}N$ core-shell nanowires grown by PAMBE (32-03-706)

K. Hestroffer, H. Renevier, C. Leclere, B. Daudin (CEA Grenoble)

Using the INS instrument of the beamline IF, our first objective was to understand the process of nucleation of GaN nanowires grown by Plasma Assisted Molecular Beam Epitaxy. The questions we aimed at answering were related to the very first stages of the GaN nanowires growth. What happens on the Si surface when exposed to Ga and N simultaneously? When exposed to N only? When exposed to Ga only? What conditions make the start of nucleation possible? How is it related to the Ga flux involved?

Our second aim was to monitor *in situ* the evolution of strains involved when depositing an AlN shell around these GaN nanowires.

**Nucleation**

Although it wasn't included in the proposal we submitted, this part of the work we performed was the most successful one. As a matter of fact, we discovered that when exposed to the slightness beam of active nitrogen, the Silicon surface is nitridated. This nitridation consists in the formation of a crystalline structure detectable by its corresponding peak in the reciprocal space (Fig. 1). Interestingly, the intensity of such peak increases and very quickly (less than 1 minute after the start of the nitridation process) saturates. Then, when further exposed to N (up to 10 minutes), the intensity of the peak remains constant. Such a surface was afterwards simultaneously exposed to Ga and N. We noticed that a *sine qua non* condition for the GaN to start growing (i. e. for the peak related to crystalline GaN to appear) is the decrease of the intensity of the peak related to nitridated Silicon (Fig.2)

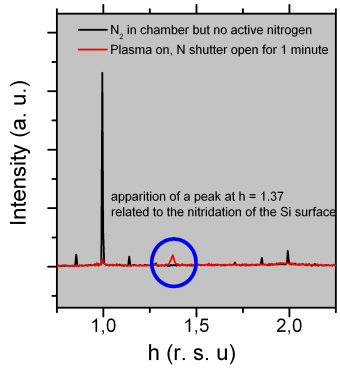


*Fig. 1. h-scan around* $(1\ 0\ 0)_{Si}^{hex}$ *before (black line) and after (red line) turning on the plasma. Without the presence of active nitrogen, one can see the typical Si 7x7 reconstruction. With the introduction of active nitrogen, the 7x7 has disappeared and a peak at h = 1.37 has shown up. This peak is related to the formation of crystalline* $Si_xN_y$.

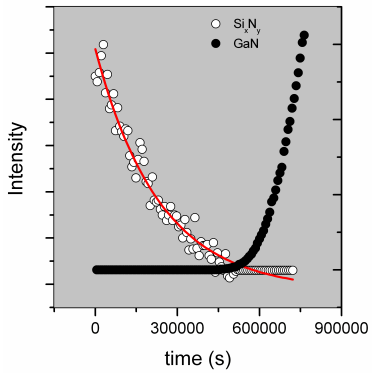


*Fig. 2. Evolution in time of the peak related to crystalline* $Si_xN_y$ $(1.37\ 0\ 0)_{Si}^{hex}$ *and of the peak related to GaN* $(3.62\ 0\ 0)_{Si}^{hex}$ *while depositing Ga and active N.*

This decrease was first understood as the destruction of the crystalline layer but later on, rather interpreted as an amorphisation of the layer. Interestingly, no matter how important the Ga flux is, the SiN peak always takes more or less the same time to disappear. An other interesting result is the fact that even when attempting to protect the silicon surface by leaving it under a constant Ga flux prior to the turning on the plasma cell, the nitridation happens anyway.

On the other hand, when playing with AlN, the behaviour is totally different. AlN is often used as a buffer layer to improve the nanowires orientation. It is usually grown by alternatively supplying Al and N. In this case, it was interesting to observe that although the surface is covered with aluminium, the SiN related peak appears and almost instantly its intensity fades. Once the thin AlN buffer was grown (corresponding to about 40s of deposited Aluminium), it was also observed that the GaN nanowires start growing much faster than on bare Silicon (about 5 minutes on AlN VS 2h00 on bare Silicon in this case)

**Strains in core-shell nanowires**

The requirements for a successful measurement of non –biased strains in core-shell nanowires are the following: straitness of the GaN cores, homogeneity of the shell thickness from nanowire to nanowires and symmetry of the shell on a given nanowire. Such features were supposed to be obtained by performing Selective Area Growth, which is being able to properly control the density of nanowires and therefore better managing their final morphology. However, prior to the experiment, it was not possible to perform such growth and therefore to determine the appropriate growth conditions. As a consequence, we decided to attempt growing a core-shell sample on bare Silicon. It can be seen from the pictures below (Fig. 3) that the nanowires are too dense and the shell totally inhomogeneous along the nanowire length. The measured strains are therefore difficult to interpret.

*Fig. 3. Scaning Electron Micrographs of the GaN/AlN core shell nanowires grown during the experiment*

## 3.2.3 Étude de la structure et des déformations locales d'une couche de graphène de haute qualité épitaxiée sur un cristal d'Ir(111). Utilisation de cette couche comme gabarit pour l'auto organisation de nanoparticules (SI 2193 + 20110422)

N. Blanc, G. Renaud, O. Ulrich (CEA Grenoble); J. Coraux, C. VoVan, F. Jean, O. Geaymond (CNRS, Institut Néel)

La croissance de graphène sur métal est connue comme la voie la plus efficace pour la production de couches de graphène de haute qualité sur de grandes dimensions [1]. Ceci explique l'engouement technologique international (par exemple Samsung, Hitachi) en vue d'utiliser ces couches comme électrodes transparentes pour l'affichage ou leur utilisation dans la production d'énergie photovoltaïque. D'un point de vue fondamental, l'étude de couches de graphène de haute qualité représente un intérêt concernant l'étude de leur croissance en vue de mieux la contrôler et donc d'en améliorer la qualité, comprendre et contrôler la structure électronique du graphène et son interaction avec le cristal sous-jacent, comprendre et contrôler des structures hybrides composées de nanoparticules ouvrant des perspectives nouvelles concernant le magnétisme, la catalyse et l'optique.

Une grande partie des propriétés du graphène est affectée par des défauts dans sa structure (par exemple des joints de grain). Le transport électrique, la conduction thermique ou la résistance mécanique de la couche peuvent êtres affectés par de tels défauts. Au contraire, d'autres peuvent êtres favorisés tel le magnétisme, qui peut être révélé par des

défauts ponctuels, ou encore l'ouverture d'un gap induit par un champ de déformations inhomogènes. Cette étude, basée sur une caractérisation structurale haute résolution de graphène sur Ir(111), met en valeur des déviations de faible amplitude par rapport à une couche parfaite (publie soumise à Phys. Rev. Lett.).

Dans un premier temps, il s'est agi de caractériser la structure de la couche de graphène en épitaxie sur Ir(111), un temps de faisceau (temps ESRF) à été consacré à cette tache avec des mesures de diffraction en incidence rasante donnant accès au paramètre de maille projeté de la couche, aux largeurs de domaine cristallographiques, à la cristallinité et enfin aux champs de déformation du graphène, le tout en fonction des paramètres de croissance, de la température d'étude. Ce temps de faisceaux fait l'objet d'une publication en cours de révisions :

# Lattice matching and local deformations in high quality epitaxial graphene

Nils Blanc,[1] Johann Coraux,[2,*] Chi Vo-Van,[3] Alpha T. N'Diaye,[3] Olivier Geaymond,[3] and Gilles Renaud[3]

[1] *CEA-UJF, INAC, SP2M, 17 rue des Martyrs, 38054 Grenoble Cedex 9 – France*
[2] *Institut NÉEL, CNRS & Université Joseph Fourier – BP166 – F-38042 Grenoble Cedex 9 – France*
[3] *II. Physikalisches Institut, Universität zu Köln, Zülpicher Str. 77, 50937 Köln – Germany*

(Dated: November 15, 2011)

We show that epitaxial graphene, even of the highest quality, displays tiny imperfections over distances of several 10 nm. X-ray diffraction and scanning tunneling microscopy reveal strains, rotations and shears. We provide insights into the nature of graphene epitaxy on a metal it weakly interacts with, here iridium. The graphene structure can be tailored by tuning the temperature. Accurate control of the growth temperature appears decisive for reproducible preparation of graphene.

Graphene growth at the surface of low-carbon solubility metals like Ir, Pt or Cu stops once the surface is passivated by a full graphene layer. It is thus a straightforward route to single-layer graphene preparation, which opened the route to the production of large-area, highly conductive graphene electrodes [1]. Structural defects forming during growth, for instance grain boundaries [2], hinder the improvement of graphene's performances (*e.g.* for electronic transport, heat conduction, mechanical resistance) towards state-of-the-art ones obtained in exfoliated, suspended graphene. Recently, ultra-high vacuum (UHV) investigations allowed for deepening the understanding of the processes governing graphene growth on metals [3–9] and avoiding the formation of grain boundaries, in graphene having single crystalline orientation at the scale of a centimeter [10]. Certain defects are on the contrary desirable: some point defects are expected to switch on magnetism in graphene [11], and inhomogeneous strain fields were shown to induce electronic gap opening [12]. Gaining knowledge about the nature of defects is hence of fundamental importance.

We address a system, graphene/Ir(111), which is a case study example of high quality graphene weakly interacting with a metal [13], thus a playground for the engineering of the band structure of graphene (see Ref. 14 for instance). Conditions preventing the formation of small- and large-angle grain boundaries in graphene [10] were used. We report high resolution structural characterizations of graphene/Ir(111) which unveil small, unanticipated deviations to a perfect graphene lattice and provide insight into the nature of the epitaxy.

X-ray diffraction with synchrotron light was conducted inside the UHV growth chamber, under grazing incidence to achieve maximum sensitivity to the graphene overlayer; scanning tunneling microscopy (STM) was performed in a separate system [15].

The room temperature (RT) lattice parameter of isolated graphene –a conceptual object– was calculated to be $a_{C,RT} = 2.4565$ Å [16]. This is several percents larger than the lattice parameter of most dense-packed transition metal surfaces, a mismatch which cannot be accomodated by graphene due to its high stiffness [17]. So-called moirés having a few nanometer period result. These moirés proved especially sensitive to small displacements and rotations of the graphene lattice [18]. We analyzed the in-plane structure of graphene and the moiré by exploring an in-plane cut in reciprocal space (Fig. 1a).

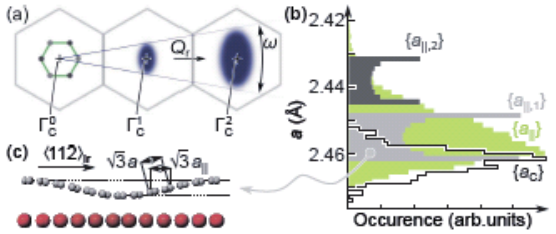


FIG. 1. (Color online) (a) First to third graphene BZs and their center ($\Gamma_C^{0\to 2}$). Scattered intensities at $\Gamma_C^{1,2}$ (blue ellipses) are characterized by azimuthal ($\omega$) and radial ($Q_r$) FWHMs. (b) Distributions of graphene lattice parameter, $\{a_C\}$ (black line), of in-plane projections, $\{a_{\parallel,1,2}\}$, for two $a_C$ values (light and dark grey), and of the projected values, $\{a_\parallel\}$ (green), for all lattice parameters in $\{a_C\}$. (c) Side-view along a ⟨112⟩ direction in Ir illustrating the nanorippling-induced $\{a_{\parallel,1}\}$ for a given $a_C$ and the periodic strain in the last Ir plane (red).

At locations where Ir crystal truncation rods (CTRs) or graphene rods intersect the in-plane cut of the reciprocal space, intensity maxima are found. For the Ir CTR passing through the center ($\Gamma_{Ir}^2$) of the third Brillouin zone (BZ), the re-

sult is shown in Fig. 2a (see Ref. 15 for the second BZ). The Ir(111) single crystal yields a sharp contribution reflecting its high quality. Besides the Ir peaks, a graphene contribution is also observed (at $\Gamma_C^2$), whose position yields the RT in-plane projection of the lattice parameter of graphene, $a_{\parallel}$=2.4543±0.0005 Å. This is substantially larger than the value (2.4453 Å) expected for a commensurate phase with 10 graphene cells matching 9 Ir ones. Since nanorippling is expected with a typical amplitude $s$=0.5 Å over 25 Å [13], due to the weak, varying interaction between graphene and Ir as a function of the location in the graphene/Ir moiré, the actual lattice parameter in graphene on Ir ($a_C$) should be slightly larger (Figs. 1c), typically 0.3% for a sinusoidal height modulation. This yields $a_C$=2.4617 Å, which should be considered as an average lattice parameter (see later), and is only 0.2% larger than the $a_{C,RT}$=2.4565 Å value [16] for isolated graphene. This is consitent with the very limited charge transfer between graphene and Ir, typically 0.01 electron or hole per atom [13]. By contrast, a much larger $a_{\parallel}$ = 2.4895 Å value is found in graphene/Ru(0001) [19], yielding $a_C$ 2% larger than $a_{C,RT}$ taking nanorippling (sinusoidal, $s$=1.5 Å over 30 Å [20]) into account, consistent with the strong electron doping [21] of graphene on Ru.

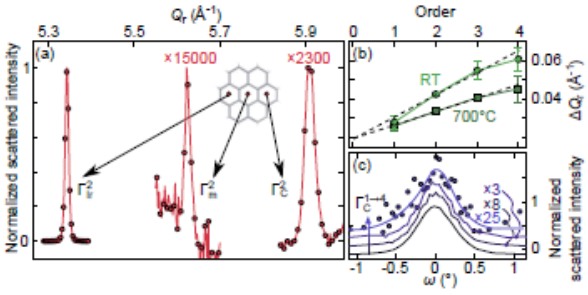


FIG. 2. (Color online) (a) Radial scans at RT close to the third BZ center for Ir ($\Gamma_{Ir}^2$) and graphene ($\Gamma_C^2$), revealing a moiré peak ($\Gamma_m^2$). (b) Graphene radial scans FWHMs ($\Delta Q_r$) as a function of peak order ($\Gamma_C^{1\to4}$), at RT and 700°C, obtained after deconvolution from the Ir peak FWHM and the experimental resolution function, and linear fits (dashed lines). (c) Azimuthal angle ($\omega$) scans for graphene at $\Gamma_C^{1\to4}$, vertically shifted for clarity. For $\Gamma_C^4$ a fit (solid line) to the data (disks) is shown.

A moiré peak, labeled $\Gamma_m^2$ in Fig. 2a, is found halfway between the Ir ($\Gamma_{Ir}^2$) and graphene ($\Gamma_C^2$) peaks, corresponding to a $a_m$=25.6±0.2 Å period. This peak is a signature of local periodic variations of the metal-graphene interaction, as shown later in this paragraph. Higher order moiré peaks, which are revealed by electron diffraction [22] thanks to extreme surface sensitivity and multiple diffraction, are here not detectable [15]. This agrees with the weak graphene-Ir interaction. Assuming a small periodic strain in Ir (sketched in Fig. 1c with a color gradient for Ir atoms), of amplitude $\varepsilon$, caused by the local graphene-Ir interactions, the position of the $i$-th Ir atom in a chain is given by $a_{Ir}(i+\varepsilon\cos(2\pi i a_{Ir}/a_m))$. Summing up the contribution of all Ir atoms to the scattered amplitude accounts for the observed moiré peaks. This holds for both commensurate and incommensurate lattices. Second order commensurability, with 25 graphene unit cells matching 23 metal ones, was proposed for graphene/Ru(0001) [19]. The closest high order (second and third) graphene/Ir(111) commensurate structure would consist of 21 graphene unit cells matching 19 metal ones, which is yet slightly but significantly off the $a_m$ and $a_{\parallel}$ values. A description in terms of a single commensurate or incommensurate graphene/Ir(111) phase is too naive as we shall see.

The line-shapes of the graphene in-plane diffraction peaks reveal the subtle nature of the graphene-Ir epitaxy. Radial and angular widths of the $\Gamma_{Ir}^{1\to4}$ Ir peaks are identical (0.01 Å$^{-1}$ and 0.08° respectively). Along the radial direction, the graphene peak width increases linearly with peak order from $\Gamma_C^1$ to $\Gamma_C^4$ (Fig. 2b). This radial broadening originates *per se* from in-plane strains. The most obvious strain pertains to the periodic graphene-Ir interaction. Periodic modulations of in-plane lattice parameter in graphene are indeed expected because the graphene nanorippling induces a periodic variation of the in-plane projection of the carbon bonds (Fig. 1c). However, these periodic strain fields yield the observed satellite (moiré) peaks but do not induce peak broadening [23].

The slope of the radial width increase as a function of peak order provides an estimate of the full width at half maximum (FWHM) of the lattice parameter distribution, sketched in Fig. 1b, 0.009±0.003 Å. Extrapolation to zero gives the typical size of the structurally coherent graphene domains, 70±50 nm. This size could be that of graphene domains each having different strains (Fig. 3a). These domains could be high order commensurate phases (first order commensurate phases have too high strain to contribute to the graphene and moiré peaks), and

possibly also incommensurate phases. Alternatively, several 10 nm domains, commensurate, thus pinned to the Ir(111) lattice, all having the same strain, but separated by domain walls [24], could also account for the observations. The strain field in these walls fixes their size: the 0.009 Å FWHM suggests that one (or 1/3 or 2/3 if the domains are located on different terraces) Ir(111) lattice parameter is accomodated in a few 100 graphene unit cells, *i.e.* typically 100 nm (Fig. 3b).

By contrast with the radial direction, the graphene peaks are constant in angle (0.53°), as seen in Figs. 1a and 2c, which indicates that small-angle disoriented and/or sheared domains are also present.

If these disorientations, shears, and strains were extending at large range, they should be reproduced by the moiré with a ca. 10-fold amplification [18], which would yield moiré peaks 10 times wider than the graphene ones. Instead, the (first order) moiré peak is about twice narrower (0.015 $Å^{-1}$ and 0.26° FWHM) than graphene ones in both radial and angular directions. This is actually expected if the domains affected by the structural fluctuations extend only over a few moiré periods at most. In this case indeed, the structural fluctuations are actually local displacements of the moiré sites with respect to an average lattice, which yields only diffuse scattering and no peak broadening [23]. The aforementioned models, small, several-10 nm domains having different strains, and a single kind of small domains separated by large, typically 100 nm-large domain walls (which may be approximated by slices, with size a fraction of the wall, each having constant strain), are both relevant.

The scanning probe microscopy observation of the structural fluctuations is certainly hindered by the need for atomic resolution and distortion-less imaging over several 10 nm, a challenging task. In the present study, an attempt to detect these fluctuations by STM could only reveal shears, in both graphene and moiré lattices (Fig. 3c).

The origin of the structural fluctuations is speculative. We propose that the balance between flexural modulus, reactivity with Ir (and as a consequence, tendency to accommodate heteroepitaxial stress) and van der Waals interaction with Ir leads to a large number of shallow energy minima or metastable states with different nanorippling amplitudes, carbon bond lengths, shears, or in-plane orientations. The coexistence of different graphene phases was already reported in the case of large-

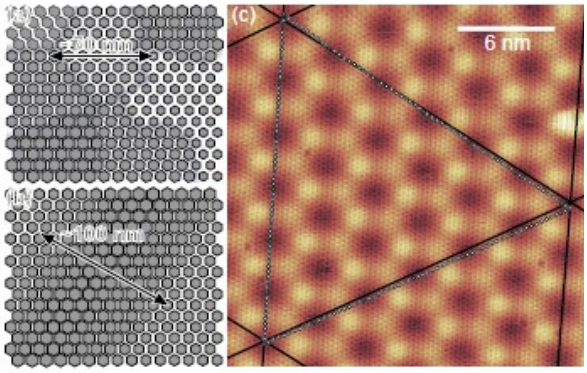


FIG. 3. (Color online) (a,b) Graphene deformation mapped onto a regular mesh with hexagons at its nodes, whose shapes represent amplified deformations (strain, rotation, shear), for two cases: ca. 70 nm domains, each having distinct deformation (a), and a domain wall (ca. 100 nm) between two domains having the same deformation. (c) STM topograph of graphene/Ir(111). Solid lines follow the moiré lattice, white dots mark centers of carbon rings. The two triangles share only one edge, evidencing an in-plane shear.

angle orientation variants in graphene/Ir [6]. Here we propose that growing graphene domains accumulate elastic energy until a critical size, for which forming a domain wall becomes favorable. The alternative scenario, pointing to a contribution of (larger) domain walls could be favoured by the pinning of the walls by substrate defects like atomic step edges. The estimate for several 10 nm domains separated by 100 nm walls would correspond to the average distance between these defects, as estimated with atomic force microscopy [15].

The average epitaxial matching of graphene on Ir(111) can be tuned by varying the growth temperature ($T_g$). Figure 4a shows a graphene peak (red) whose position corresponds to $a_{\parallel}$=2.4470± 0.0005 Å, 0.3% smaller than the previous value. Taking nanorippling into account as before yields $a_C$=2.4548 Å, which is less than 0.1% of the expected value for isolated graphene. The accuracy of our temperature probe (±60°C) does not allow detecting difference in $T_g$ between the two samples. In order to further test its influence, $T_g$ was varied over 200±60°C (Fig. 4b), resulting in variations of $a_{\parallel}$ by almost 0.01 Å. The dependence of $a_{\parallel}$ on $T_g$ is not trivial: configurations with longer or shorter carbon bonds and more or less nanorippling can be stabilized at low and high $T_g$. The observed varia-

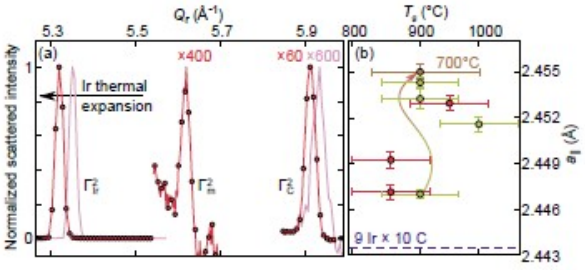


FIG. 4. (Color online) (a) Radial scans close to the third BZ center at 700°C (light red), and the same sample decorated with Pt clusters [15] at RT (red). (b) Spread of in-plane projections, $a_{\parallel}$, of $a_C$, measured at RT, as a function of $T_g$, for two series of measurements (yellow and red data points). The value for a commensurate phase with 9 Ir cells matching 10 graphene ones is displayed. The orange point corresponds to a sample grown at 900°C and studied at 700°C.

tion suggests that graphene experiences some biaxial stress from the substrate during growth.

Besides $T_g$, the sample temperature also influences the epitaxial matching: while between RT and 700±60°C the Ir lattice parameter is expanded by 0.48%, for graphene $a_{\parallel}$ is increased by only 0.33%, from 2.4470±0.0005 to 2.455±0.001 Å (Fig. 4a,b). This is much more than estimated from first principle calculations [25]. The thermal expansion coefficient (TEC) of graphene is here yet not vanishing as it is expected for free-standing graphene in this temperature range [16]. The weak tendency to periodic chemical bonding in graphene/Ir [13] appears to induce a partial inheritance, in graphene, of the Ir TEC. The two TECs yet differ [26], suggesting some slippage of graphene on Ir(111) against temperature-induced stress, presumably due to the high stiffness of graphene. Taking nanorippling into account as before, $a_C$ is 0.3% larger than the expected lattice parameter ($a_{700}$=2.4556 Å) for isolated graphene at this temperature [16], while at RT for this sample, the deviation to the expected $a_{RT}$ value was less than 0.1%. The superperiodicity is slightly decreased, to a value of 24.5±0.2 Å. The radial scans width (Fig. 2c) increases with peak order, yet to a lesser extent than at RT. The angular widths are also constant (0.43°), smaller than at RT. Hence, various epitaxial matchings or domain walls are present also in graphene at 700°C, but they differ from the RT ones in that the associated graphene lattice parameter spread is narrower. The fact that no wrinkle is expected, when the temperature differs from $T_g$ by less than 400°C [27], supports the previous proposal that inhomogeneities develop during growth, and not only upon wrinkle formation.

The carbon bond length in graphene on Ir(111) is very close to that of isolated graphene, at most a few 0.1% larger. Detailed analysis reveals small local deformations in graphene, domains separated by domain walls, which form upon growth. Either the domain extension should be several 10 nm, or the domain walls should extend over typically 100 nm. Further study of these structural fluctuations could make use of the expected resulting particle or quasiparticle scattering, phonon modes, local charge transfers and chemical inhomogeneities, processes which steer many of graphene's properties. Intercalation of species suppressing the non-vanishing graphene-metal interaction, like alkali metals or hydrogen, could yield truly free-standing graphene where the structural inhomogeneities could be released. Temperature is found very efficient in tailoring the structure of graphene, which could allow for epitaxial control of its properties.

We thank T. Michely and C. Busse for STM measurements and fruitful discussions. C. V.-V. acknowledges support from the Fondation Nanosciences. Research supported by EU NMP3-SL-2010-246073 "GRENADA" and French ANR ANR-2010-BLAN-1019-NMGEM contracts.

* johann.coraux@grenoble.cnrs.fr

[1] X. Li et al., Science **324**, 1312 (2009).
[2] P. Y. Huang et al., Nature **469**, 389 (2010).
[3] E. Loginova, N. Bartelt, P. Feibelman, and K. McCarty, New J. Phys. **10**, 093026 (2008).
[4] J. Coraux et al., New J. Phys. **11**, 023006 (2009).
[5] K. F. McCarty, P. J. Feibelman, E. Loginova, and N. C. Bartelt, Carbon **47**, 1806 (2009).
[6] E. Loginova, N. Bartelt, P. Feibelman, and K. McCarty, New J. Phys. **11**, 063046 (2009).
[7] E. Loginova et al., Phys. Rev. B **80**, 235422 (2010).
[8] J. Lahiri et al., Nano Lett. **11**, 518 (2010).
[9] S. Günther et al., Nano Lett. **11**, 1895 (2010).
[10] R. van Gastel et al., Appl. Phys. Lett. **95**, 121901 (2009).
[11] O. V. Yazyev, Phys. Rev. Lett. **101**, 037203 (2008).
[12] N. Levy et al., Science **329**, 544 (2010).
[13] C. Busse et al., Phys. Rev. Lett. **107**, 036101 (2011).
[14] R. Balog et al., Nature Mater. **9**, 315 (2010).
[15] See supplementary material at [URL will be inserted by AIP] concerning measurement conditions, atomic

force microscopy and electron diffraction characterizations of the samples, details about the X-ray data analysis, the effect of Pt cluster grown on graphene, and attempts for measuring higher order moiré peaks.
[16] K. V. Zakharchenko, M. I. Katsnelson, and A. Fasolino, Phys. Rev. Lett. **102**, 046808 (2009).
[17] C. Lee, X. Wei, J. Kysar, and J. Hone, Science **321**, 385 (2008).
[18] J. Coraux, A. T. N'Diaye, C. Busse, and T. Michely, Nano Lett. **8**, 565 (2008).
[19] D. Martoccia et al., Phys. Rev. Lett. **101**, 126102 (2008).
[20] B. Wang et al., Phys. Chem. Chem. Phys. **10**, 3530 (2008).
[21] P. Sutter, M. S. Hybersten, J. T. Sadowski, and E. Sutter, Nano Lett. **9**, 2654 (2009).
[22] P. Langer et al., New J. Phys. **13**, 053006 (2011).
[23] A. Guinier, X-ray diffraction in crystals, imperfect (Dover Publications, 1994).
[24] P. Bak, Rev. Prog. Phys. **45**, 587 (1982).
[25] M. Pozzo et al., Phys. Rev. Lett. **106**, 135501 (2011).
[26] This difference is probably underestimated, graphene probably being flatter at higher temperature due to tensile epitaxial stress, which is known for instance to cause wrinkles to disappear [27].
[27] A. T. N'Diaye et al., New J. Phys. **11**, 113056 (2009).

Par la suite, du temps de faisceau alloué par le comité français a été consacré à l'étude du graphène comme gabarit pour l'auto organisation de nanoparticules. Dans un premier temps une étude de l'organisation de plots d'or à été réalisée (avec et sans intercalation d'or entre le substrat et le graphène), puis une deuxième expérience à été menée sur des particules magnétiques à forte anisotropie : l'alliage CoPt (dépôt alterné de platine puis de cobalt). Le dépôt est contrôlé *in situ* par GISAXS (Fig. 1) et diffraction dans le plan (Fig. 2). Pour les nanoparticules de platine, par exemple on voit en diffraction qu'il n'y a aucune modification de la projection dans le plan du paramètre de maille du graphène après dépôt (fig. 2). On voit en GISAXS, outre l'évolution de la taille, que les nanoparticules à la surface du graphène sont organisées avec un réseau hexagonal au pas équivalent au graphène nu (fixation des atomes sur les sites hcp du graphène).

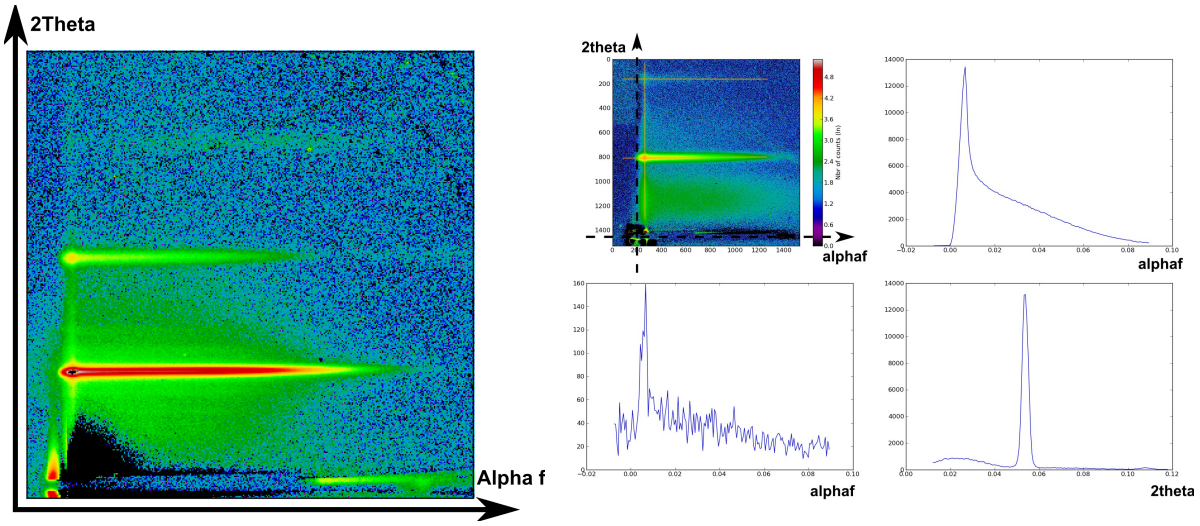


*Figure 1 :Image GISAXS d'un dépôt auto organisé de 0,6ML d'or (gauche) et de 0,13ML de platine (droite). Le montage de droite fait apparaître le traitement en vue de déterminer par ajustement avec le logiciel IsGISAXS les dimensions des plots.*

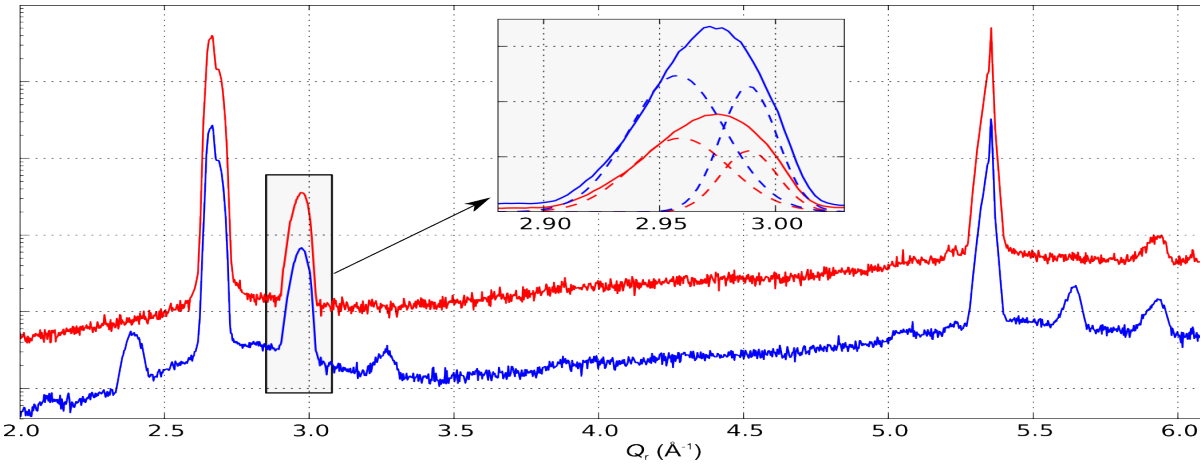


*Figure 2 : Spectres de diffraction dans le plan (scan radial) en rouge le graphène nu et en bleu avec 0,13ML de platine sur la surface.*

### 3.2.4 In-situ study of the compliant interface growth of Ge on $SrTiO_3$ (SI 2094)

G. Saint-Girons, B. Gobaut, A. Chettaoui, J. Penuelas (INL-ECL, Lyon) ; V. Favre-Nicolin, G. Renaud, N. Blanc (CEA-Grenoble)

The objective of the experiments is to study the growth of Ge on SrTiO3 (STO) substrates. Ge/STO is a model of very heterogeneous epitaxial system that has potential application in the field of microelectronic. The structural properties are very dependent of the nature of the interface between Ge and STO.

The flux of the Ge evaporator was calibrated at 1.6A/minute via a quartz microbalance, which correspond to an evaporation temperature of 1190°C. This flux is low enough to be able to follow each step of the growth (typically few seconds of deposition and then GIXD + GISAXS measurements). SrTiO3 substrates were degased, and the surface reconstruction observed via RHEED and GIXD in order to obtain a clean surface. However we were not completely satisfied of the commercial substrate quality (XPS measurements performed after the experiment has shown lots of impurity in $SrTiO_3$). However a clean 2x1 surface was obtained after annealing at 550°C. The substrate temperature during the deposition was calibrated. At high temperature (>550°C) Ge re-evaporate and we cannot grow the layer, the only way to avoid this re-evaporation is to grow a Ge thick layer. The substrate temperature was then changed to 430°C, a successful growth was then performed corresponding to 370s of Ge deposition.

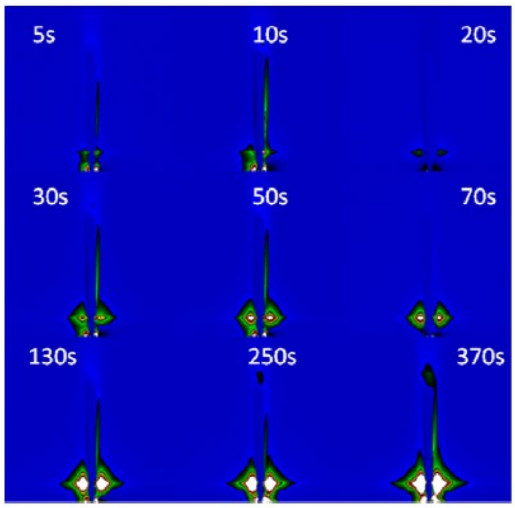


*Figure 1 : GISAXS pattern (background subtracted) during the Ge deposition.*

A mapping of the reciprocal space was performed in order to identify each contribution ("bulk like" $SrTiO_3$ , $SrTiO_3$ surface reconstruction, 111 oriented Ge and 001 oriented Ge). On this mapping we identify, the Ge Bragg peaks corresponding to two different orientations. We decided to follow the evolution of these peaks during the growth. At each step GISAXS measurements were performed for three different azimuths corresponding to

different sample orientations, in order to observe any effect of the surface anisotropy (step, surface reconstruction domain).

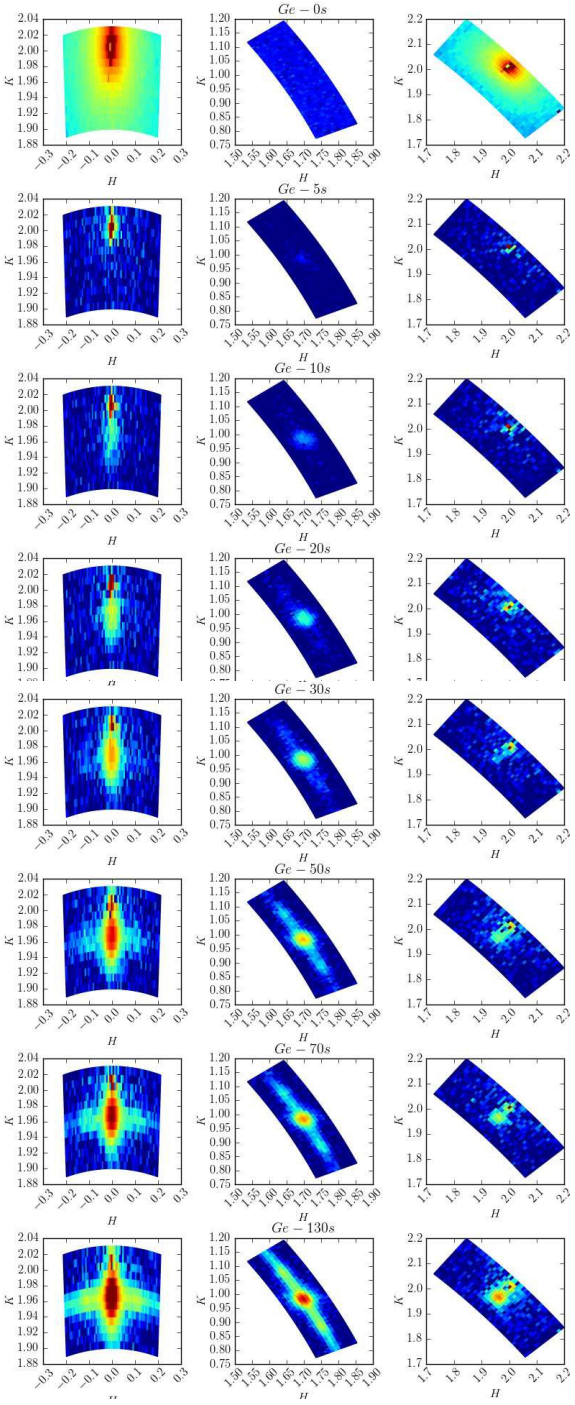


*Figure 2 : Evolution of the reciprocal space map during the Ge deposition*

The evolution of the GISAXS pattern shows the formation of two lobes which is the signature of nucleation and subsequent growth of Ge islands on the surface. No island faceting is visible, the patterns corresponding to the three azimuthal angles show no clear differences, which means no surface anisotropy is detected via GISAXS. DWBA simulations are in progress with the IsGISAXS software [1] in order to extract the islands morphology (diameter, height, and shape), the evolution of the islands density will be also determined.

Mappings of the Bragg peaks located around h=2, k=0 (first column); h=1.7, k=1 (second column) and h=2, k=2 (third column) are shown on figure 2 in $SrTiO_3$ reciprocal space units. The first and second columns are related to 220 Ge Bragg peak and the third to the 400 Ge Bragg peak. Each line corresponds to different Ge deposition time. Figure at 0 s correspond to the substrate, then the data are corrected of the substrate contribution.

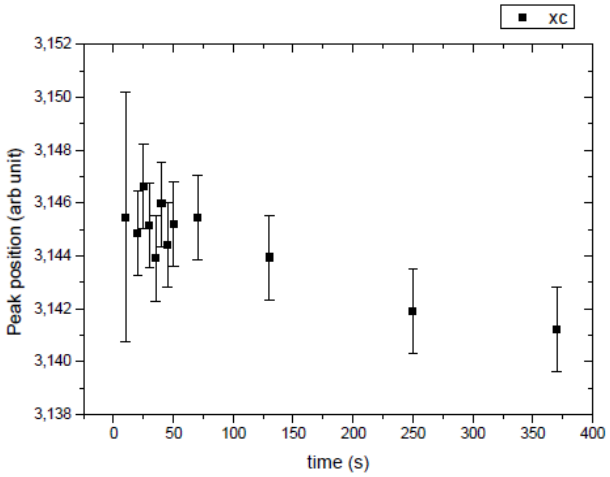


*Figure 3:Evolution of the position of Ge 220 peak with time*

From these data we extracted the Ge Bragg peak (first column) which was fitted with Voigt function. The position and the width of the peak was determined and plotted with the deposition time (figure 3).

At the very beginning of the growth we observed that the lattice parameter of Ge is slightly different from the bulk which could be the signature of interfacial dislocation. However due to important substrate contribution, the fit is difficult and error bars are important.

By performing l-scans we could measure the Ge lattice parameter and avoid the substrate contribution. This contraction of the Ge lattice parameter could be the signature of strains at the very beginning of the growth, during the formation of the dislocation network at the Ge/SrTiO3 interface. Analysis is still in progress.

Two kinds of islands were observed, corresponding to two different epitaxial relationships. The first one is related to a cube on cube epitaxy leading to 001 out of plane oriented Ge islands, the other one is related to triangle on square epitaxy leading to 111 out of plane oriented Ge islands. The mappings of figure 2 are related to these islands: first column to 001 + 111 islands, second column to 111 islands, third column to 001 islands.

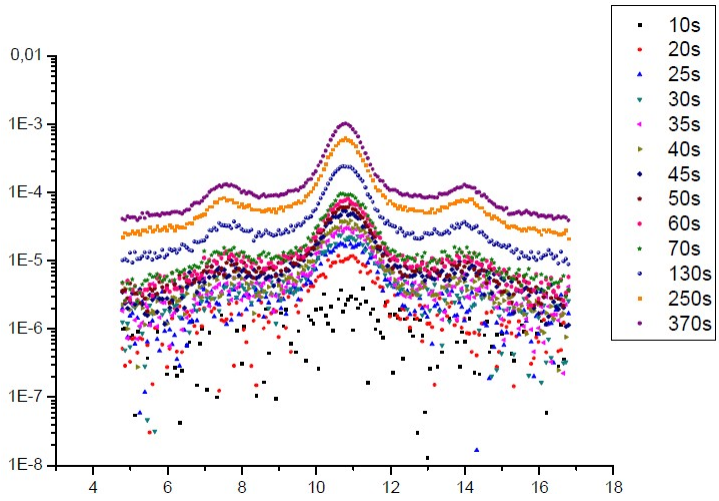


*Figure 4: Azimuthal scans for a Ge(220) reflection corresponding to 111 oriented islands.*

The volume of each peak is being analyzed in order to obtain the proportion of these two kinds of islands during the growth. Interestingly 111 oriented islands correspond to incommensurate epitaxy. However several orientations seem to be favorable as displayed on figure 4 which represents azimuthal scans around the 220 Ge Bragg peak. This effect was already observed for InP on $SrTiO_3$, and was explain by a simple model [2], however the measurements were performed at a fixed amount of InP. Our results show the evolution of these preferential orientations with the particles size. Calculations are in progress to fit our data.

References:

[1] R. Lazzari, Journal of Applied Crystallography **35**, 406 (2002)
[2] G. Saint-Girons et al. Applied Physics Letters **92**, 241907 (2008)

### 3.2.5 Interface structure of Ge islands on $SrTiO_3$ (SI 2412)

J. Penuelas , G. Saint-Girons, B. Gobaut (INL-ECL, Lyon) ; V. Favre-Nicolin, N. Blanc, G. Renaud (CEA-Grenoble)

The objective of this experiment is to study the structural properties of small amount of Ge on SrTiO3 (STO) substrates. It is a continuation of the experiment Si-2094.

At the beginning of the run, we analyzed the surface reconstruction of $SrTiO_3$ during the heating from room temperature to 750°C. Three STO substrates from different companies were prepared at the chemistry lab following a method describe in reference [1] and were then introduced in the UHV chamber. Interestingly we observed behavior depending on the substrate nature. Some substrate do not reconstructed properly despite annealing at temperature higher than 800°C. We decided to work with substrate having the best surface reconstruction. The formation of the 2x1 surface reconstruction was followed by RHEED and Grazing Incidence X-ray Diffraction (GIXRD).

Ge was then deposited on the reconstructed $SrTiO_3$ surface at a temperature of 490°C during few seconds, then the sample was cooled to room temperature and measured by GIXRD. For each deposition sequence a set of 6 Bragg peaks were measured for several Ge orientations corresponding to different epitaxial relationship. In order to extract in plane and out of plane Ge lattice parameter hkscan and lscan were performed, and rocking scan (omegascan) were performed to follow the islands twisting during the growth.

a. Three different epitaxial relationship

From the measurements, three different epitaxial relationships were reported. Interestingly these three epitaxial relationships exhibit a common axis: the Ge[110] axis is aligned with the STO [100] axis . This axis seems to drive the epitaxy of the Ge on the STO system. The misfit in this direction is 2.43% and is accommodated by dislocation network confined at the interface.

The growth kinetic of these three islands family is under progress in order to understand which kind of islands nucleates first and if there is transformation of one islands family to another during the growth. As suggested by photoemission results obtained at TEMPO beamline at SOLEIL.

Formation of the 111 islands twist:

From our previous experiment we know that 111 islands twist on the STO surface. This effect was measured during the growth as shown in figure 2.

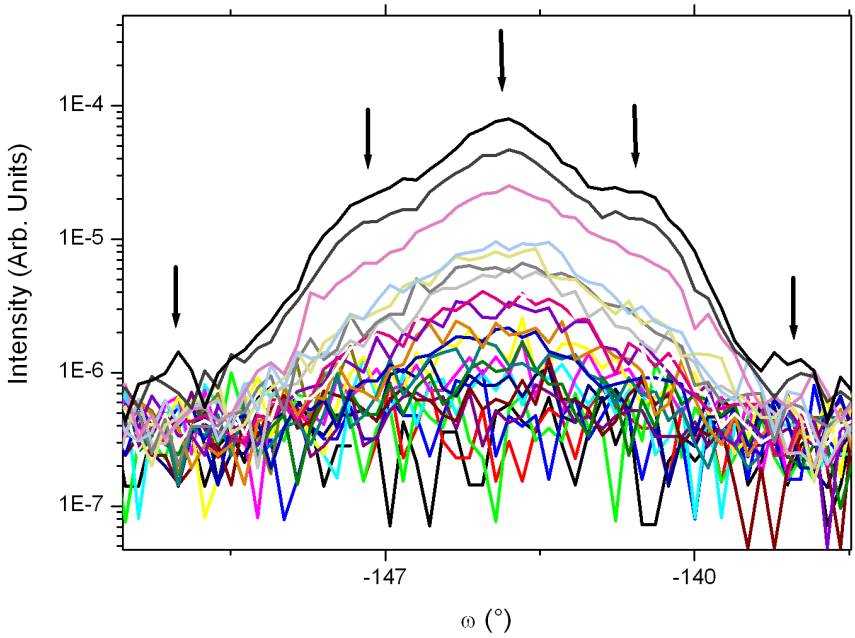


*Figure 2: Sequence of rocking scan performed during the growth (without cooling the sample, nor closing the Ge shutter) for 111 oriented Ge islands. At the end of the growth the strongest peak is related to a triangle on square epitaxy with one side of the triangle parallel to one side of the square. Other peaks are marked by arrows, they are related to islands twist due to a minimization of the interfacial energy.*

A simple model, based on Keating interaction, is in progress in order to simulate our results.

Mismatch accommodation through the dislocation network:

The lattice parameter of these islands has been extracted from the data by fitting the Bragg peak. The figure 3 shows the evolution of the lattice parameter for islands having a size between 1 and 30 nm. At the very beginning of the growth, the Ge lattice parameter corresponds to a fully strained Ge on $SrTiO_3$. At the end of the deposition we obtained a fully relaxed Ge corresponding to bulk lattice parameter. This relaxation is due to the formation of the dislocation network confined at the interface of Ge/STO system. This behavior is being modeled by an atomistic model, using a Frenkel potential.

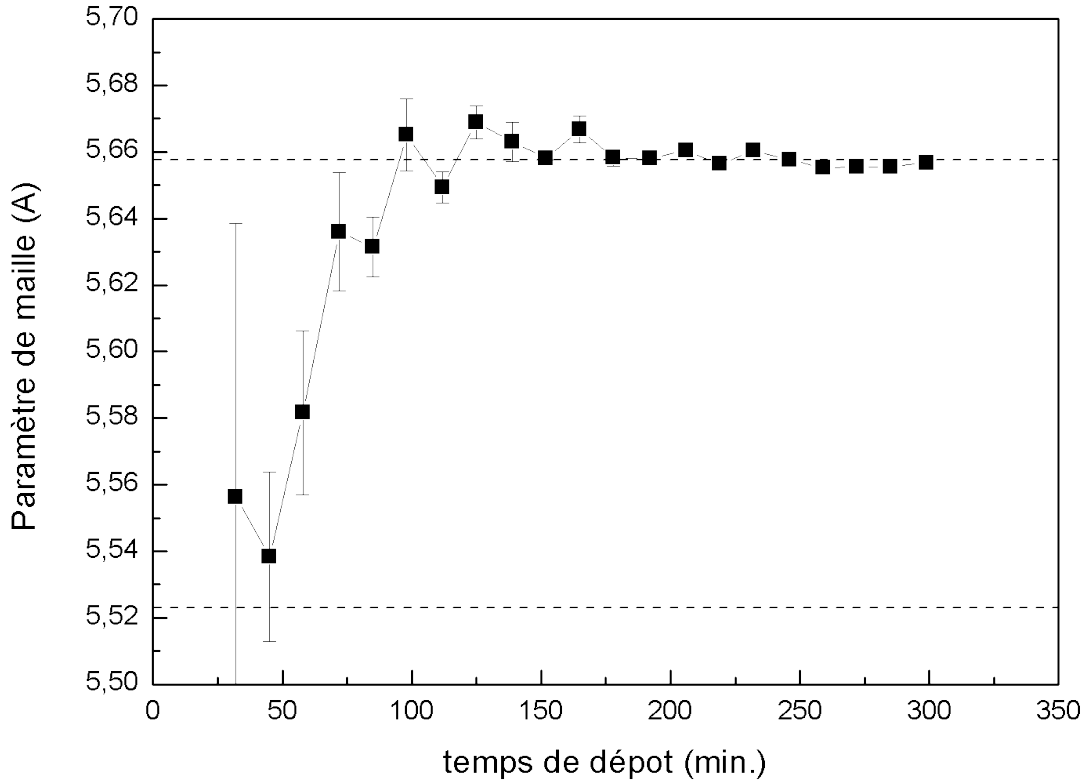


*Figure 3: Evolution of the in plane lattice parameter of 001 Ge oriented islands with the deposition time. The broken line at 5.52A corresponds to fully strained Ge, and fully relaxed Ge at 5.66A.*

### 3.2.6 In-situ study of the $SrTiO_3$/Si system (32-03-707)

B. Vilquin , G. Saint-Girons, J. Penuelas, G. Niu, B. Gobaut S. Yin (INL-ECL, Lyon)

This experiment was aimed at studying the early stages of the growth of STO/Si by means of surface diffraction, and obtaining state of the art information on the structure of the (1x2) and (1x3) SrSi reconstructions used for Si surface passivation. For studying the SrSi reconstructions, Sr was deposited on a bare and clean Si surface following the procedure commonly used prior to STO growth. Diffraction rods from the SrSi reconstructions were recorded, and they will be fitted and compared with ab-initio calculated surface models

As second step, in- and out-of plane diffraction was used to measure the lattice parameters of 3 and 7 monolayer thick STO/Si layers as well as their evolution during annealing under vacuum and under different oxygen partial pressures.

For 3 monolayer thick films, two STO phases are present and that they are both strained on Si, thus contradicting the interpretation published by Schlom et al. that one of the two STO phases is formed during plastic relaxation.

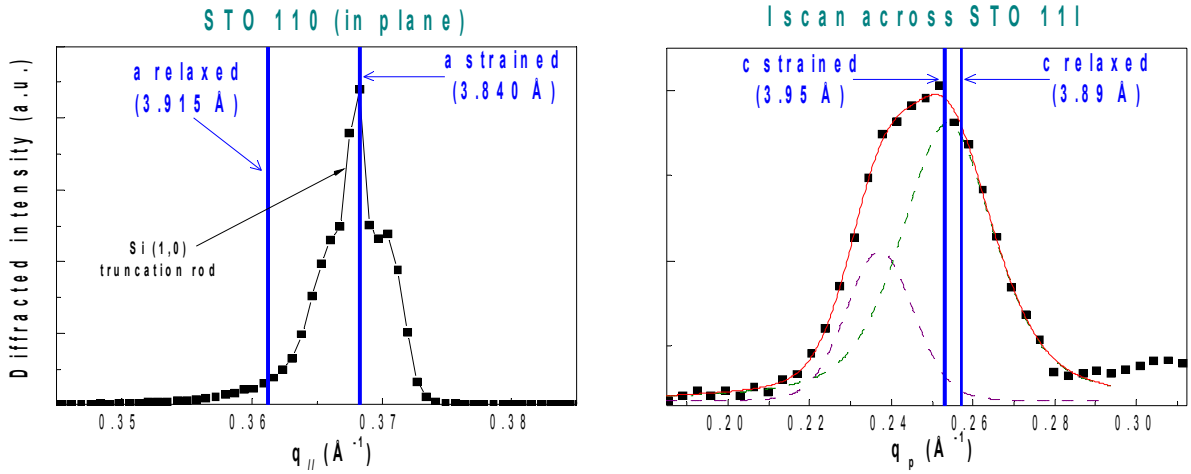


These experiments also show clearly that one of the two STO phases is standard cubic STO, fully strained up to at least 3 ML, and that the other phase is also cubic, and formed due to deficient oxidation conditions. In the end, STO is not ferroelectric as shown by our temperature dependent lattice parameter measurements.

The data analysis is in progress, it should allow for concluding on the detailed atomistic structure au the SrSi passivation layer deposited prior to STO growth and on the space group of the O-deficient STO phase (using diffraction extinction rules) and the origin of its formation.

### 3.2.7 Correlation between structural properties and magnetic behaviors of $Fe_{1-x}Co_x$ thin films grown on Rh(001) and Pd(001) surfaces (SI 2092)

M. Przybylski, F. Yildiz, R. Bali (MPI, Halle, D), M. Soares (CNRS, Institut Néel)

The authors used the surface preparation and electron beam deposition techniques at the UHV X-ray diffractometer to gather information on the growth of $Fe_{1-x}Co_x$ ($0 < x < 0.5$) alloys. Grazing incidence X-ray diffraction (GIXRD) using 22 keV photons has been employed to optimize the growth route and to measure the crystallographic structure (in-plane and out-of-plane lattice parameters) as function of the coverage and composition on Rh(001) and Ir(001). In the case of the Rh(001) substrate, three different compositions were studied (x=0, 0.25, 0.5). A short experiment was done, in addition, on the Ir(001) crystal for the composition x=0.5.

The deposition rate was calibrated for both Fe and Co using a quartz balance. For the x=0.5 sample the calibration was at about 1ML/18min. At each stage of the growth the *c/a* ratio was determined. At the end of each thin layer preparation, the composition was checked by Auger spectroscopy. A summary of the main results that has been found up to now (further analysis is required) are given below (see figure):

<u>For the deposition of $Fe_{1-x}Co_x$ alloys on Rh(001), is was got:</u>

x=0.5 (figure, red squares):

There is no in plane layer relaxation at all, i.e., the in-plane parameter of the $Fe_{50}Co_{50}$ alloy is strictly the same as that of Rh crystal up to 19 ML. The interlayer spacing decreases with increasing thickness and reaches the nearly saturated value of c=3.181 Å above 12-14 ML. This gives a $c/a$=1.18A and a cell volume of 11.50 $Å^3$.

The analysis has been based on a model where the d-spacing – or c/2 – is the same for the whole thin layer, except for the d-spacing between the Rh surface and the first alloy layer. The blue point (figure) at 1 ML represents that value, which is almost independent on the layer thickness.

x=0.25 (green circles):

The thin layer displays a similar behavior at that composition. However, the layer starts to relax around 8-10 ML, where the ($c/a$) is about 1.20. One can observe that the ($c/a$) (green circles) is larger for all unrelaxed (up to 10 ML) thickness compared to x=0.5 (red squares) which is expected because there is more Fe in the composition.

Pure iron : Qualitatively, we observed a similar behavior with a decreasing ($c/a$) as thickness increases. In addition, a clear relaxation process starts around 6 to 8 ML. As for x=0.25, the relaxation process is gradual. A quantitative fitting involving both relaxed and unrelaxed phases has to be done.

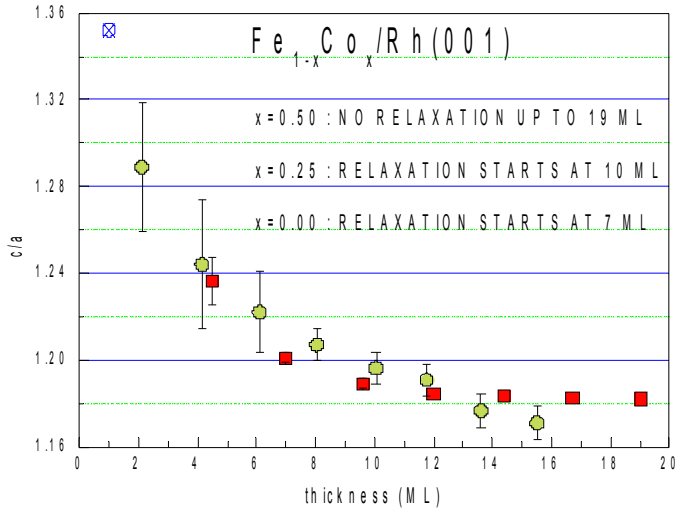


For the $Fe_{1-x}Co_x$/Ir(001), we have obtained some preliminary qualitative results. Pure Fe grows pseudomorphically up to about 8 ML and then starts to relax; the in-plane parameter relaxes to 2.745 Å ($a_{Ir}$=2.715 Å) and the out-plane parameter to 3.16 Å, giving a ($c/a$)=1.15 after relaxation around 8ML.

During the deposition of the x=0.5 alloy, the Co deposition rate was extremely stable. However, the Fe source decreased slowly, giving a composition with an excess in Co. The film started to relax around 12-13 ML. The final sample with about 18 ML gave an in-plane parameter of 2.753 Å and an out-plane of 3.012 Å, giving a ($c/a$)=1.09. The magnetic phase diagram (Co content versus thickness) of the $Fe_xCo_{1-x}$ alloy on Ir(001) is rather complex, and this structural data needs the support of theoretical calculations to to explain the observed magnetic properties.

### 3.2.8 Growth mode and correlation between structural and magnetic properties of ultra-thin Fe layers on Ag(001) (32.3.705)

H. C. N. Tolentino, M. M. Soares, M. De Santis, A. Y. Ramos (CNRS, Institut Néel)

Scope and expected results:

The aim of this experiment was to investigate the correlation between structural and morphological properties and magnetic behaviors of ultra-thin Fe films deposited on Ag(001) single-crystals. The most interesting property of the Fe/Ag(001) system is the spin reorientation transition (SRT) as function of the thickness and temperature. This system might be an interesting candidate in spintronic studies, for instance when coupled with antiferromagnets in an exchange-biased CoO/Fe/Ag(001) bilayer or by being controlled with an external electric field.

We want to solve the question concerning the first steps of the growth mode (Frank – van der Merwe (layer-by-layer), Welmer – Weber (3D) or Stranski – Krastanov (layer-by-layer followed by 3D)) of Fe/Ag(001) and get quantitative information on structural and morphological aspects in the 0 – 3 ML range. The epitaxial conditions and interlayer spacing ($c/a$ ratio) will be precisely determined in a wide range of coverage, in particular within the spin reorientation transition (SRT). This will teach us which parameters are the more relevant for the perpendicular magnetic anisotropy. We expect to verify the limit of the pseudomorphic growth and the relaxation of the structure for high coverage and to see if there is any correlation with the magnetic properties. It is known that for constant thickness (4 to 6 ML) the SRT takes place by moderate heating above room temperature. We will check if there is any counterpart in the structural aspects. A surfactant effect, even if incipient, is an aspect that could come out from such diffraction experiments and could be eventually an important piece in the knowledge of the properties.

Experimental results:

The first steps of Fe growth on Ag(001) was studied in situ by GIXRD at IF (BM32) beamline. Beam energy of 22 keV was used. The films were grown at room temperature, to minimize intermixing, then moderate annealing, up to 470 K, was done to improve the quality of the surface and modify morphological aspects. The growth was followed in real time along the (1 -1) crystal truncation rod (CTR) - to track the perpendicular lattice parameter $c$ - and in the plane (h,k) scanning across the (1 -1 2.7) and (1 -1 2.83) positions in reciprocal space - to confirm (or infirm) the pseudomorphic behavior. Complete sets of CTRs were measured for some particular coverage. This allows solving the structure and getting accurate lattice parameters. We present here some remarkable outcomes. A complete quantitative analysis has not been done, yet.

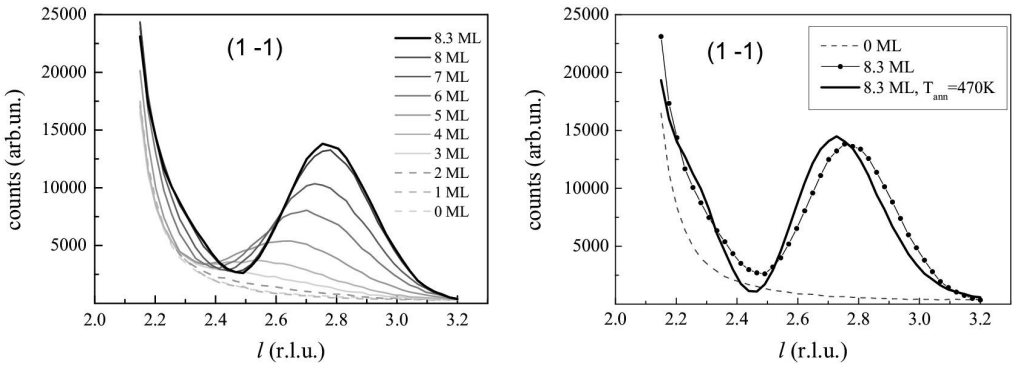

*Figure 1 (a) Real time evolution of the (1 -1) CTR during the Fe deposition. (b) (1 -1) CTR before and after annealing the 8.3 ML Fe film on Ag(001).*

At room temperature, the magnetic easy axis of Fe/Ag(001) changes from out-of-plane to in-plane around 6 MLs. By tracking the in-plane lattice parameter of the deposited layer up to 8, 11 and 14 ML, in three different depositions, and even after annealing at 470 K, we could eliminate a possible relaxation of the Fe film as an explanation for the SRT: the Fe films grow pseudomorphically taking the in-plane lattice parameter of Ag, which is larger than the bulk bcc Fe by 0.8%. Interestingly, however, the *c/a* does not become smaller than one, as it would be expected after pseudomorphic growth at constant volume.

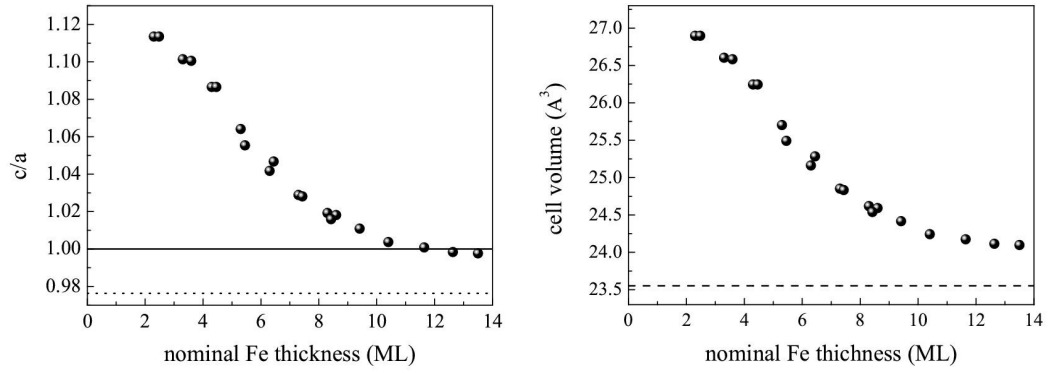


*Figure 2 : (a) Tetragonal distortion as function of coverage; the solid line gives the limit of no distortion; the dotted line gives the situation where the volume of the unit cell would be the same as bulk bcc Fe. (b) volume of the unit cell for the Fe film as function of the coverage. The dash line gives the volume of the bulk Fe bcc.*

The real time evolution of the (1 -1) CTR during Fe on Ag(001) deposition for a up-to-8.3 ML film is presented in figure 1-a. Tracking the peak position yields a good average estimation of the *c/a* value. In figure 2-a, we present the estimation of the tetragonal distortion for two different experiments, namely for the up-to-8 and up-to-14 ML depositions. One clearly sees that the distortion is larger than one up to about 10 ML. Nevertheless, we must emphasize that the in-plane parameter is that of Ag(001) and, even above 10 MLs where *c/a* is close to one, the volume of the Fe layer unit cell is still larger than for bulk Fe. In figure 2-b one can observe the evolution of the cell volume at different coverage. For very low coverage, the average cell volume of Fe films is larger by about 14%.

One additional comment concerns the annealing at 470 K that is often mentioned in the literature. This is normally done to improve the morphology by reducing the surface roughness. Fe and Ag have a high degree of immiscibility and this would help to separate a possible presence of Ag in the Fe layer. In figure 1-b we show the effect of the annealing on the (1 -1)CTR for the 8.3 ML film. The annealing reduce the roughness, as seen from Kiessig oscillations (not shown), and has the effect of increasing the *c* lattice parameter, while keeping the pseudomorphism (no changes in plane lattice parameter). In addition, from Kiessig oscillations (not shown) we observe that the initial rough surface is thicker than the nominal value but decreases after annealing. Auger electron spectroscopy showed an increased amount of Ag at the surface compared to Fe after the annealing.

To summarize, we verified the limit of the pseudomorphic growth and demonstrated that there is no relaxation of the Fe films up to coverages of 14 MLs, and even after mild annealing at 470 K. We obtained the variation of the tetragonal distortion as function of the Fe coverage and observed that the unit cell volume is always larger than bulk. It is known that for constant thickness (4 to 6 ML) the SRT takes place by moderate heating above room

temperature. We have shown that the structural counterpart is an increase of the tetragonal distortion and the appearance of a surfactant layer of Ag.

These results are part of the PhD thesis of Marcio M. Soares (UJF, 2011) http://tel.archives-ouvertes.fr/docs/00/60/37/54/PDF/Soares_Marcio_2011_archivage_1_.pdf

### 3.2.9 Exchange coupled CoO / FePt ultra-thin films grown on Pt(001)

A. Lamirand, M. De Santis, H. C. N. Tolentino, M. M. Soares, A. Y. Ramos (CNRS, Institut Néel)

During this experiment we have elaborated *in situ* a layered system by growing ~3 nm of CoO on an ultra-thin (about 1.5 nm thick) PtFe layer on Pt(001). The PtFe layer is chemically ordered with the tetragonal $c$ axis perpendicular to the surface and in coherent epitaxy. The average c/a ratio is about 0.93, smaller then the bulk value (0.96) We have already shown that this distortion is associated with an enhanced orbital magnetism (M. M. Soares et al., J. Appl. Phys. 109, 07D725 (2011)). The oxide structure corresponds in a first approximation to a CoO(111) film, with large roughness. A deeper structural study reveals a clear monoclinic distortion.

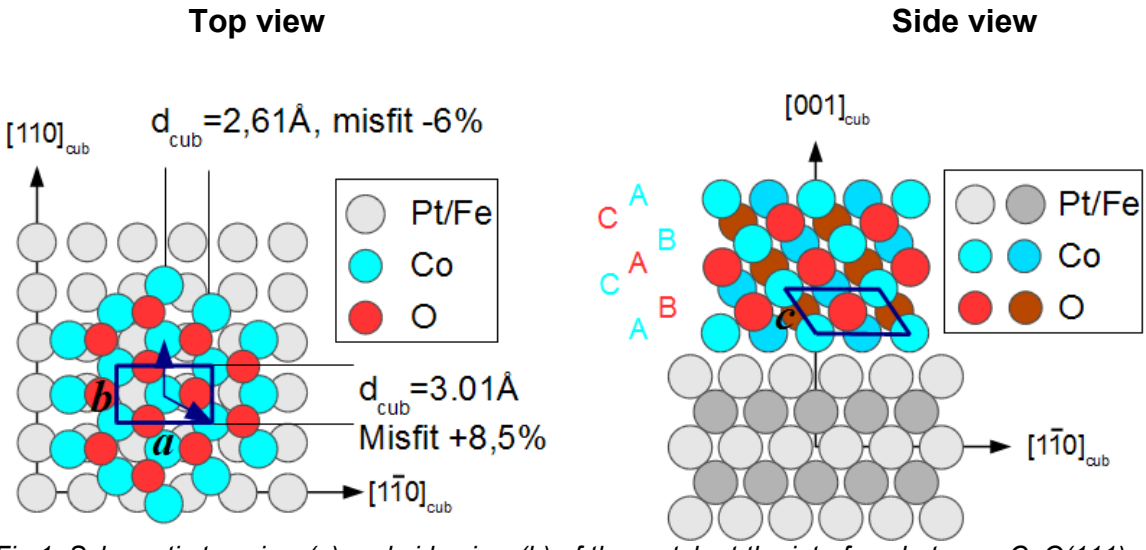


*Fig.1: Schematic top view (a) and side view (b) of the match at the interface between CoO(111) and Pt(001).*

Figure 1 shows how CoO(111) and PtFe(001) film structure could match at the interface. Four of these domains are observed in diffraction owing to the symmetry of the substrate. Due to the anisotropic stress, the induced strain on the AFM film results in a slightly distorted cubic structure, which is then described by a monoclinic cell (space group *C2/m*) like the bulk CoO low temperature phase. This distortion is clearly evidenced by the comparison between the experimental (-1 0) and (0 1) rods of the hexagonal surface cell. These rods are equivalent in the cubic and non-equivalent in the monoclinic structure. In the experimental data a shift is clearly observed (Fig. 2) which corresponds to the fact that the $c$ axis for the hexagonal surface cell is no more perpendicular to the surface.

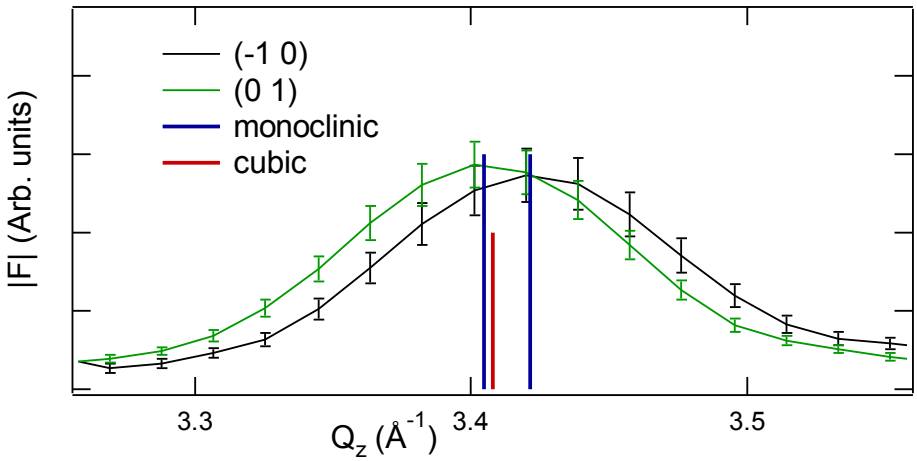


*Fig. 2. Comparison between the (-1 0) and (0 1) rods of the CoO(111) hexagonal surface mesh measured on the CoO/PtFe/Pt(001) sample.*

Such a distortion observed at room temperature is of the same order of magnitude as the one of the low temperature bulk phase. However, the monoclinic *bc*-plane results compressed instead of expanded. This difference would possibly give rise to a modification on the antiferromagnetic behavior of the layer.

The system shows perpendicular magnetic anisotropy and exchange bias after field cooling from room temperature.

The results of this experiment have been presented at the ECOSS-28 conference, Wroclaw, 28 August-2 September 2011, and are part of the PhD thesis of Anna Lamirand (UJF), which started this year.

### *3.2.10 In-situ* X-ray scattering investigations of the UHV-CVD growth of Si and Ge nanowires .

*Valentina Cantelli, Tao Zhou, Gilles Renaud*

Nanoscale one-dimensional materials have been stimulating great interest thanks to their unique mechanical, thermoelectric, and optical properties relative to their bulk counterparts. Typically, Si NWs are grown via the Vapour – Liquid - Solid (VLS) mechanism, in which nanowires (NWs) spring up from catalyst-substrate eutectic droplets (AuSi) under flux of silicon fuelled by the decomposition of CVD (Chemical Vapour Deposition) precursor gases.

The main problems affecting the NW production are related to the wide diameter size distribution and to the non homogeneity in growth direction (tapering, kink, diameter expansion), clearly a consequence of the not deep understanding of the effect of the crystallography at the early stage of the growth. Identifying the lattice parameter relaxation and epitaxial relations between the NW and the substrate will probably be a valuable tool to control NW growth direction and shape. This motivated the launch of a project, funded by the Nanoscience Fundation, to investigate the growth of semiconductor NWs by Ultra-High Vacuum Chemical Vapour Deposition (UHV-CVD), at the end station INS of IF-BM32 beamline, combining the UHV-MBE set-up with CVD able to completely follow the growth of silicon and germanium NWs using silane ($SiH_4$), germane ($GeH_4$) and disilane ($Si_2H_6$) gas precursors. The first *in-situ* growth of Si NWs started in April 2011 corresponding to this experiment, which aim was the determination of the crystallographic properties of Si NWs with respect to the growing conditions, gas pressure and substrate temperature.

The early stages of NW nucleation were studied by exposing Ge(111) substrates to $Si_2H_6$ flux at different temperatures between 400 and 550°C: the *in-situ* growth at 470°C is reported in figure 1, as example.

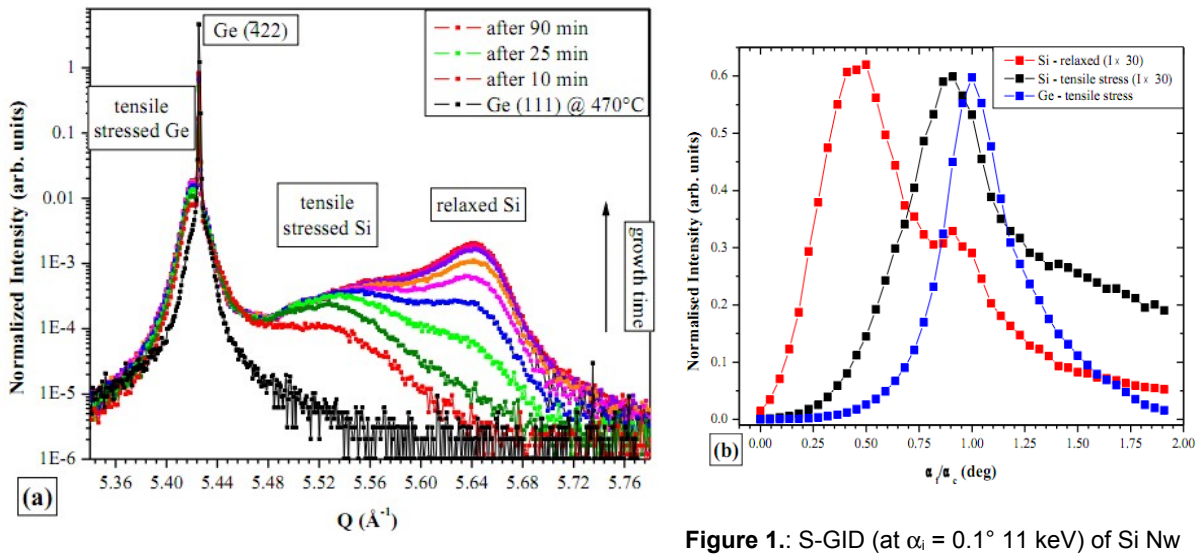


**Figure 1.**: S-GID (at $\alpha_i$ = 0.1° 11 keV) of Si Nw growth on Ge(111) substrate at 470°C – 2 ML of Au under $Si_2H_6$ at 0.3 sccm, 90 min of deposition.

As soon as the silicon precipitation occurred, clearly detected after 10 min at a $Q \cong 5.54$ Å$^{-1}$, the Ge surface reacted resulting in stretch of the surface in-plane lattice parameters. At the early stages of NW formation, Si precipitates are characterised by a compression of the in-plane lattice parameters (peak at the right of the Ge(-422) Bragg

reflection in fig. 1-a). The relaxed Si component, for Q ≅ 5.66 Å$^{-1}$ is unambiguously observed only after 25 min of growth (figure 1-a). Both the compressed and the relaxed Si have the same in-plane crystallographic orientation of the substrate.

At the end of the growth, the exit angle $\alpha_f$ curves were measured (figure 1-b) for the three signals detected by the radial scan of fig. 1-a. The position of the curve maximum can be correlated with the height *z*, above the Ge substrate, of the corresponding component [2]. For the relaxed Si signal, $\alpha_f^{max}/\alpha_c$ (experimental Ge $\alpha_c$ = 0.22°) is at 0.46, corresponding to *z* = 12 nm.

The GID pattern collected during exposition of Si(111) substrate to $Si_2H_6$ are reported in figure 2.

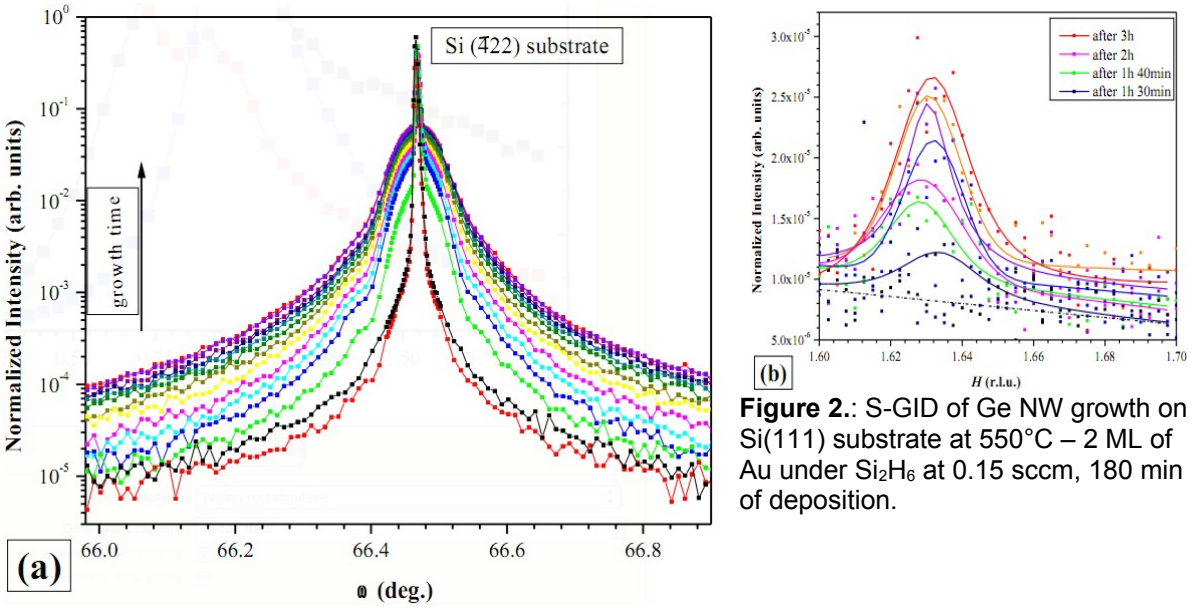


**Figure 2.**: S-GID of Ge NW growth on Si(111) substrate at 550°C – 2 ML of Au under $Si_2H_6$ at 0.15 sccm, 180 min of deposition.

In contradiction with other studies [3, 4], we do not observe any remarkable expansion of the in-plane lattice parameters of the NWs with respect to the substrate (figure 2-a). On the contrary, the large contribution of the Si from the NW results to be well aligned with the substrate. But, in-plane stacking faults were detected at $(1.67\ 1.33\ 0)_S$ with the development of the growth, after 90 minutes. We suppose that the in-plane stacking faults appearance could be related with the formation of a kink into the NW: the evolution of the integral area of this reflection can therefore give an indication of the NW "kink rate" during growth at these particular conditions of temperature and pressure.

*Ex-situ* Scanning Electron Microscopy (SEM) investigations are reported in figure 3.

The micrograph of the Ge(111) substrate (figure 3-a), after exposition to $Si_2H_6$, do not show the presence of NWs. Nanoclusters of Si are observed having maximum size of approximately 50 nm, with no preferential growth direction and surrounded by a rough 2D layer.

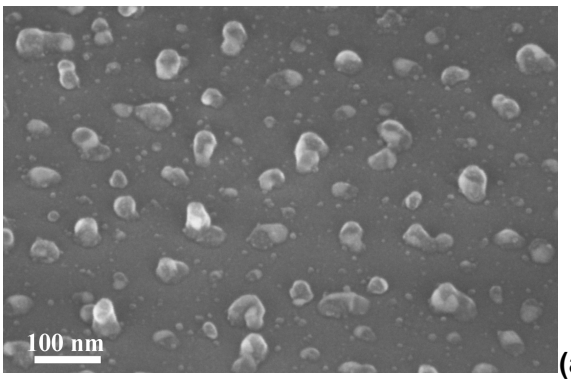

**(a)**
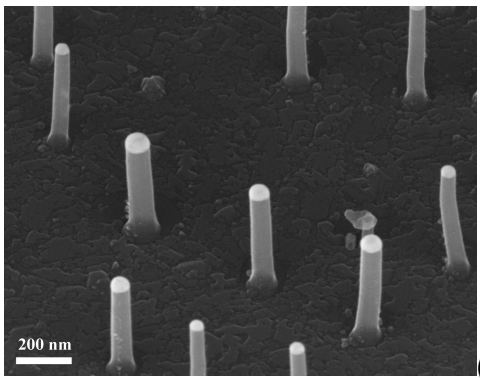

**(b)**

**Figure 3.**: *Ex-situ* SEM after growth recorded at 45°angle of incidence . a) Ge(111) substrate exposed to $Si_2H_6$ (0.3 sccm, 90 min) at 470°C b) Si(111) substrate exposed to at 550°C $Si_2H_6$ (0.05 sccm, 180 min of deposition).

Completely different is the result obtained exposing Si(111) with 2ML of gold to $Si_2H_6$ (Fig. 3-b). The majority of the NWs seems to be quite straight, characterised by a larger hexagonal base on which it is possible to identify au droplets. Also in the case of Si substrates the reaction of $Si_2H_6$ with the bare substrate caused the formation of a rough layer surrounding the NWs.

References:

[1] F. M. Ross, Rep. Prog. Phys. 73 (2010) 114501
[2] I. Kegel *et al.* Phys. Rev. Lett. 85 (2000) 1694
[3] T. David *et al.* Surf. Science 602 (2011) 2675
[4] D. Buttard *et al.* Surf. Science 605 (2011) 570

# 4 Publications

**Articles les plus cités et publiés depuis cinq ans (2006-2011)**

| | |
|---|---|
| Thelander et al, Materials Today, 2006 | 237 |
| Verilhac et al, Synthetic Metals, 2006 | 57 |
| Nolte et al, Science, 2008 | 49 |
| Renaud et al, Surface Science Report, 2009 | 47 |
| Schülli et al, Nature, 2010 | 35 |
| Eymery et al, Nano Letters, 2007 | 28 |
| Sousbie et al, J. Appl. Phys., 2006 | 22 |
| Minkevich et al, Phys. Rev. B, 2007 | 21 |
| Revenant et al, Nucl. Instr. Meth. B, 2006 | 21 |
| Landré et al, Nanotechnology, 2009 | 20 |
| Benedetti et al, Phys. Rev. B, 2008 | 20 |

**Nombre de publications (comité de lecture) par année**

| | |
|---|---|
| 2009 | 16 |
| 2010 | 19 |
| 2011 | 22 ( au 15 Novembre) |

**Articles publiés depuis trois ans (2009-2011) dans des revues à fort impact (index>3)**

| | | |
|---|---|---|
| Nature | 35 | 1 |
| Surface science Reports | 18 | 1 |
| Physical Review Letters | 7.2 | 1 |
| Chemical Comm. | 5.6 | 1 |
| Electrochem. Comm. | 4.9 | 1 |
| J. Phys. Chem | 4.7 | 3 |
| Acta Materialia | 4.4 | 3 |
| Faraday Disc. | 4.3 | 1 |
| J. Appl. Cryst. | 4.2 | 1 |
| Appl. Physics Letters | 3.9 | 4 |
| NanoTechnology | 3.8 | 2 |
| Physical Review B | 3.4 | 10 |

Les publications relatives à l'utilisation de BM32 sur la période 2009-2011 sont classées par année et par ordre décroissant du facteur d'impact de la revue.

[] facteur d'impact de la revue au 15/11/2011
() nombre de citations de l'article au 15/11/2011

## 2011

[12.8] *M-plane core-shell InGaN/GaN multiple-quantum-well on GaN wires for electroluminescent device*
R. Koester, J. S. Hwang, D. Salomon, X. Chen, C. Bougerol, J.-P. Barnes, D. Le Si Dang, L. Rigutti, M. Tchernycheva, C. Durand and J. Eymery
Nano Letters 11, p 4839-4845 (2011)

[5.6] *From metastable to stable modifications—in situ Laue diffraction investigation of diffusion processes during the phase transitions of (GeTe)nSb2Te3 (6 <= n <= 15) crystals*
M. N. Schneider, X. Biquard, C. Stiewe, T. Schröder, P. Urban and O. Oeckler
Chemical Communication Accepted (2011)

[4.9] *In situ grazing-incidence X-ray diffraction during electrodeposition of birnessite thin films: Identification of solid precursors*
M. Ndjeri, S. Peulon, M.L. Schlegel, A. Chaussé
Electrochem. Commun. **13**, (5) p 491-494 (2011)

[4.7] *Size and Catalytic Activity of Supported Gold Nanoparticles: An in operando Study During CO Oxidation*
I. Laoufi, M.-C. Saint-Lager, R. Lazzari, J. Jupille, O. Robach, S. Garaudee, G. Cabailh, P. Dolle, H. Cruguel, A. Bailly
J. Phys. Chem. **C 115** (11) pp 4673-4679 (2011)

[4.7] *Competition between polar and non-polar growth of MgO films on Au(111)*
S. Benedetti , N. Nilius, P. Myrach, P. Torelli, G. Renaud, H.-J. Freund, S. Valeri
J. Phys. Chem. **C 115,** 23043 (2011)

[4.4] *In situ synchrotron analysis of lattice rotations in individual grains during stress-induced martensitic transformations in a polycrystalline CuAlBe shape memory alloy*
Berveiller S., Malard B., Wright J., et al.
Acta Mater. **59** (9) p 3636-3645 (2011)

[4.4] *Impact of instrumental constraints and imperfections on the dislocation structure in micron-sized Cu compression pillars*
Kirchlechner C., Keckes J., Motz C., Grosinger W., Kapp M.W., Micha J.S., Ulrich O. and Dehm G.
Acta Mater. **59** (14) p 5618-5626 (2011)

[4.4] *Expected and unexpected plastic behavior at the micron scale: An in situ Laue tensile study*
C. Kirchlechner , P.J. Imrich, W. Grosinger, M.W. Kapp, J. Keckes, J.S. Micha, O. Ulrich, O. Thomas, S. Labat, C. Motz, and G. Dehm
Acta Mater. accepted (2011)

[4.3] *Catalytic properties of supported gold nanoparticles: new insights into the size-activity relationship gained from in operando measurements*
M.-C. Saint-Lager, I. Laoufi, A. Bailly, O. Robach, S. Garaudée and P. Dolle
Faraday Discuss., **152**, p253–265 (2011)

[4.2] *Full local elastic strain tensor from Laue microdiffraction: simultaneous Laue pattern and spot energy measurement*
O. Robach, J.-S. Micha, O. Ulrich and P. Gergaud
J. Appl. Cryst.. **44** p 688–696 (2011)

[3.9] *Effect of doping on global and local order in crystalline GeTe*
Biquard X., Krbal M., Kolobov A. V. *et al*
Appl. Phys. Lett. **98** (23) 231907 (2011)

[3.9] *In situ x-ray study of the formation of defects in Ge islands on Si(001)*
M.-I. Richard, T. U. Schülli, and G. Renaud
Appl. Phys. Lett. **99** 161905 (2011)

[3.9] *Growth of ultra-high quality GaN nanowires by catalyst-free MOVPE*
X.J. Chen, B. Gayral, C. Bougerol, C. Durand and J. Eymery
Accepted Appl. Phys. Lett.

[3.8] *Metal positioning using dislocation arrays.*
A. Bavard, F. Fournel and J. Eymery
Nanotechnology **22**, 215301(2011)

[3.4] *Twins and their boundaries during homoepitaxy on Ir(111)*
S. Bleikamp, J. Coraux, O. Robach, G. Renaud and T. Michely,
Phys. Rev. **B 83** 064103 (2011)

[3.4] *Atomic structure and composition of the 2 × N reconstruction of the Ge wetting layer on Si(001) investigated by surface x-ray diffraction*
T. Zhou, G. Renaud, J. Issartel, C. Revenant, T.U. Schülli, R. Felici and A. Malachias,
Phys. Rev. **B 83**, 195426 (2011)

[2.7] *$H_2O$ diffusion barriers at Si-Si Direct bonding interfaces for low temperature anneals*
H. Moriceau, F. Rieutord, L. Libralesso, C. Ventosa, F. Fournel, C. Morales, T. Mc Cormick, T. Chevolleau and I. Radu
J. Electrochem. Soc. **158** (9) H919 (2011)

[2.2] *Highly anisotropic epitaxial (L1)0 FePt on Pt(001)*
Soares M.M., Tolentino H.C.N., De Santis M., Ramos A.Y., Cezar J.C.
J. Appl. Phys. **109** p.07D725-1-07D725-3 (2011)

[2.0] *In Situ µLaue: Instrumental Setup for the Deformation of Micron Sized Samples*
C. Kirchlechner, J. Keckes, J.-S.Micha and G. Dehm
Advanced Engineering Materials **13** (8) p 837-844 (2011)

[1.7] *A new white beam x-ray microdiffraction setup on the BM32 beamline at the European Synchrotron Radiation Facility*
O. Ulrich, X. Biquard, P. Bleuet, O. Geaymond, P. Gergaud, J. S. Micha, O. Robach, and F. Rieutord
Rev. Sci. Instrum. **82**, 033908 (2011)

[1.5] *Water management on semiconductor surfaces*
Y. Le Tiec, C. Ventosa, N. Rochat, F. Fournel, H. Moriceau, L. Clavelier, F. Rieutord, J. Butterbaugh, and I. Radu
Microelectronic Engineering **88**, p3432-3436 (2011)

[1.4] *Dislocation storage in single slip-oriented Cu micro-tensile samples: New insights via X-ray microdiffraction*
C. Kirchlechner, D. Kiener, C. Motz, S. Labat, N. Vaxelaire, O. Perroud, J. -S. Micha, O. Ulrich, O. Thomas, G. Dehm, and J. Keckes
Phil. Mag. **91** (7-9) Special Issue p 1256-1264 (2011)

[1.4] H. Moriceau, F. Mazen, C. Braley, F. Rieutord, A. Tauzin, and C. Deguet, "Smart Cut™: review on an attractive process for innovative substrate elaboration," Nucl. Instr. Meth. B in press (2011)

[1.1] *Analysis of strain error sources in micro-beam Laue diffraction*
F. Hofmann, S. Eve, J. Belnoue, J.-S. Micha, and A.M. Korsunsky
Nucl. Instrum. Meth. A **660** (1) p 130-137 (2011)

[1.0] *Low temperature direct bonding: an attractive technique for heterostructures build-up*
H. Moriceau, F. Rieutord, F. Fournel, C. Moulet, L. Libralesso, P. Gueguen, R. Taibi and C. Deguet, Microelectronics Reliability in press (2011)

*X-Ray diffraction determination of macro and micro stresses in SOFC electrolyte and evolution with redox cycling of the anode*
Villanova J., Sicardy O., Fortunier R., Micha J.S., Bleuet P.
Materials Science Forum, vol. **681**, p.25-30 (2011)

*X-ray Diffraction analysis of elastic strains at the nanoscale*
O. Thomas, O. Robach, S. Escoubas, JS. Micha, N. Vaxelaire, O. Perroud
Chapter in “Mechanical stress on the nanoscale : simulation, material systems and characterization techniques”
Ed. : M. Hanbücken, P. Müller, U. Gösele, R. B. Wehrspohn, Wiley-VCH Books, 2011

*First stages of hydrogen implantation in silicon*
F. Rieutord, F. Mazen, J. D. Penot, L. Bilteanu, J. P. Crocombette, V. Vales, V. Holy, and L. Capello
Appl. Phys. Lett. Submitted (2011)

*Strains in light ion implanted polycrystals: influence of grain orientation*
A. Richard, H. Palancher, E. Castelier, J. S. Micha, M. Gamaleri, G. Carlot, P. Goudeau, G. Martin, F. Rieutord, P. Garcia, and J. P. Piron
Appl. Phys. Lett. Submitted (2011)

*Physics of Direct Copper Bonding*
P. Gueguen, L. Di Cioccio, F. Rieutord, F. Fillot, P. Gergaud, V. Delaye, and L. Clavelier

J. Appl. Phys. Submitted (2011)

Strains in light ion implanted polycrystals: influence of grain orientation
A. Richard, H. Palancher, E. Castelier, J.-S. Micha, M. Gamaleri, G. Carlot, P. Goudeau, G. Martin, F. Rieutord, P. Garcia and J.P. Piron
J. Appl. Cryst. Submitted (2011)

*Combining Laue microdiffraction and digital image correlation for improved stress field measurements with micrometer spatial resolution*
J. Petit, M. Bornert, F. Hofmann, O. Robach, J.S. Micha, O. Ulrich, C. Le Bourlot, D. Faurie, A.M. Korsunsky, O. Castelnau
Procedia IUTAM : Full field measurements and identification in Solid Mechanics, 2011 (accepted, page non connue)

*Growth and structure of cobalt oxide on an ultrathin PtFe epitaxial ferromagnetic layer by GIXRD*
A. Lamirand, M. De Santis, H.C.N. Tolentino, M.M. Soares, A.Y. Ramos,
ECOSS-28, 28 Aug.-2 Sep., 2011, Wroclaw.

***Thèses :***

*Plasticity at the Micron Scale: a µLaue Study*
PhD Thesis, University Leoben, Autria, 2011
Christoph Kirchlechner

*Grain level deformation studied by micro diffraction techniques*
PhD Thesis, Oxford University, United-Kingdom, 2011
Felix Hofmann

*Croissance, structure et magnétisme dans les systèmes à décalage d'échange FM/AFM : approche fondamentale par la physique des surfaces*
Thèse, Université Joseph Fourier Grenoble, France, 2011
Marcio M. Soares

***Prix – Couvertures revue:***

*In situ micro compression test studied by Laue microdiffraction*
Prix du meilleur poster
7th Winter School on Neutrons and Synchrotron Radiation, Planneralm (Austria), March 6-12, 2011
M. Kapp, C. Kirchlechner *et al*

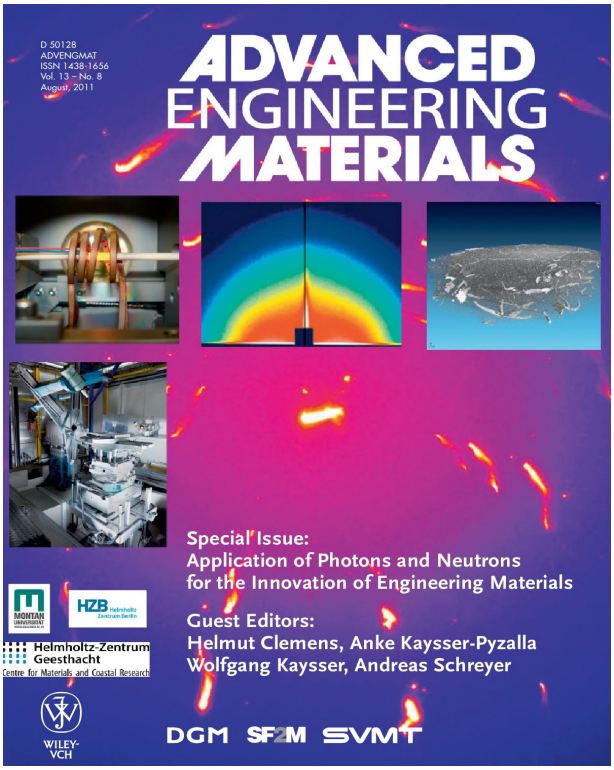


*Couverture de Advanced Engineering Materials représentant les diagrammes de Laue collectés sur BM32 (C.Kirchlechner)*

## 2010

[35] (12) *Substrate-enhanced supercooling in AuSi eutectic droplets*
T.U. Schülli, R. Daudin, G. Renaud, A. Vaysset, O. Geaymond and A. Pasturel,
Nature **464**, 1174 (2010)

[4.7] (1) *Nanoscale Patterning by C60 Ordering on Pt(110)*
Torrelles X, Langlais V, De Santis M, Tolentino HCN et al.
J. Phys. Chem. **C 114** p 15645 (2010)

[3.8] (1) *Growth, structure and magnetic properties of FePt nanostructures on NaCl(001) and MgO(001)*
Liscio F., Makarov D., Maret M., Doisneau-au-cottignies B., Roussel H., Albrecht M.
Nanotechnology **21** (6) 065602 (2010)

[3.4] (1) *Strain and correlation of self-organized Ge(1-x)Mn(x) nanocolumns embedded in Ge (001)*
Tardif S., Favre-Nicolin V., Lancon F., et al.
Phys. Rev. **B 82** (10) 104101 (2010)

[3.4] (2) Elastic strain relaxation in GaN/AlN nanowire superlattice
O. Landré, D. Camacho, C. Bougerol, Y.M. Niquet, V. Favre-Nicolin, G. Renaud, H. Renevier and B. Daudin
Phys. Rev. **B 81** 153306 (2010)

[3.4] (1) *Probing nanoscale structural and order/disorder phase transitions of supported Co-Pt clusters under*
*annealing*
P. Andreazza, C. Mottet, C. Andreazza-Vignolle, J. Penuelas, H. C. N. Tolentino, M. De Santis, R. Felici and N. Bouet
Phys. Rev. **B 82** (15) 155453 (2010)

[3.4] (6) *Highly ordered growth of Fe and Co clusters on alumina on Ni3Al(111)*
A. Buchsbaum, M. De Santis, H.C.N. Tolentino, M. Schmid and P. Varga
Phys. Rev. **B 81** (11) 115420 (2010)

[3.4] (6) *Nanostructuring surfaces: Deconstruction of the Pt(110)-(1 X 2) surface by C-60*
X. Torrelles, V. Langlais, M. De Santis, H.C.N. Tolentino and Y. Gauthier
Phys. Rev. **B 81** 041404(R) (2010)

[2.4] (2) *Confinement induced phase transition in a DNA-lipid hydrated complex*
E. Andreoli de Oliveira , E. R. Teixeira da Silva, A. Fevrier, E. Grelet, F. Nallet and L. Navailles
Europhysics Letters **91** (2) 28001 (2010)

[2.2] (4) “Supported bilayers: Combined specular and diffuse X-ray scattering”
Malaquin L, Charitat T and Daillant J
Euro. Phys. J. **E 31** p 285 (2010)
[2.2] (1) *Study of the formation, evolution and dissolution of interfacial defects in silicon wafer bonding*
S. Vincent, J. D. Penot, I. Radu, F. Letertre, and F. Rieutord,

J. Appl. Phys. **107** 093513 (2010)

[1.3] (1) *Influence of the U3O7 domain structure on cracking during the oxidation of UO2*
Desgranges, L, Palancher, H, Gamaleri, M, Micha JS., Optasanu V, Raceanu L, Montesin T, Creton N.
J. Nucl. Mat. **402** p 167 (2010)

[1.0] (4) *Determination of global and local residual stresses in SOFC by X-ray diffraction*
Villanova J, Sicardy O, Fortunier R, Micha J.S., Bleuet P
Nucl. Inst. Meth. Phys. **B 268** p 282 (2010)

*X-ray microbeam strain investigation on Cu-MEMS structures*
Perroud O, Vayrette R, Rivero C, Thomas O, Micha J.S., Ulrich O
Microelectronic Engineering **87** p 394 (2010)

*Stress field in deformed polycrystals at the micron scale*
Castelnau, O, Bornert, M., Robach, O., Micha, J. S.,Ulrich, O., Chiron, R.,Le Bourlot, C.
ICEM 14: 14th International Conference on experimental mechanics
Book Series: EPJ Web of Conferences **6** 35005 (2010)

*Defect formation at hydrophilic silicon bonding interfaces*
F. Rieutord, S. Vincent, J. D. Penot, H. Moriceau, and I. Radu,
ECS Transactions, **33** p 451(2010)

*Efficiency of H2O diffusion barriers at Si-Si direct bonding interfaces*
H. Moriceau, F. Rieutord, L. Libralesso, C. Ventosa, F. Fournel, C. Morales, T. Mc Cormick, T. Chevolleau, and I. Radu
ECS Transactions **33** p467 (2010)

*An overview of patterned metal/dielectric surface bonding: mechanism, alignment and characterization*
L. Di Cioccio, P. Gueguen, R. Taibi, D. Landru, G. Gaudin, C. Chappaz, F. Rieutord, F. de Crecy, I. Radu, L.-L. Chapelon, and L. Clavelier
ECS Transactions **33** p3 (2010)

*Single Crystal Silicon Film Transfer onto polymer*
M. Argoud, H. Moriceau, C. Fretigny, F. Rieutord, C. Morales, and L. Clavelier
ECS Transactions **33** p217 (2010)

*Overview on recent direct wafer bonding advances and applications*
H. Moriceau, F. Rieutord, F. Fournel, Y. Le Tiec, and L. Di Cioccio
in The 5th International Workshop on Advanced Materials Science and Nanotechnology (IWAMSN2010) Hanoi (2010)

## 2009

[18.0] (47) *Probing surface and interface morphology with Grazing Incidence Small Angle X-Ray Scattering*
G. Renaud, R. Lazzari and F. Leroy
Surf. Sci. Rep. **64** pp 255-380 (2009)

[7.2] (35) *Enhanced Relaxation and Intermixing in Ge Islands Grown on Pit-Patterned Si(001) Substrates*
T. U. Schülli, G. Vastola, M.-I. Richard, A. Malachias, G. Renaud, F. Uhlik, F. Montalenti, G. Chen, L.Miglio, F. Schäffler, G. Bauer
Phys. Rev. Lett. **102**, 025502 (2009)

[3.9] (4) *Multiple scattering effects in strain and composition analysis of nanoislands by grazing incidence x-rays*
M.-I. Richard, V. Favre-Nicolin, G. Renaud, T. Schülli, C. Priester, Z. Zhong and T.-H. Metzger
Appl. Phys. Lett. **94**, 013112 (2009)

[3.9] (3) *X-ray measurements of the strain and shape of dielectric/metallic wrap-gated InAs nanowires*
J. Eymery, V. Favre-Nicolin, L. Froberg and L. Samuelson
Appl. Phys. Lett. **94** 131911 (2009)

[3.9] (3) *A model of interface defect formation in silicon wafer bonding*
S. Vincent, I. Radu, D. Landru, F. Letertre, F. Rieutord
Appl. Phys. Lett. **94** (10) 101914 (2009)

[3.8] (20) *Nucleation mechanism of GaN nanowires grown on (111) Si my molecular beam epitaxy*
O. Landré, C. Bougerol, H. Renevier and B. Daudin
Nanotechnology 20 415602 (2009)

[3.4] (9) *In situ x-ray scattering study on the evolution of Ge island morphology and relaxation for low growth rate: advanced transition to superdomes*
M.-I. Richard, T. U. Schülli, G. Renaud, E. Wintersberger, G. Chen, G. Bauer and V. Holy
Phys. Rev. **B 80**, 045313 (2009)

[3.4] (3) *Defect-pinned nucleation, growth and dynamic coalescence of Ag islands on MgO(001): An in situ grazing-incidence small-angle x-ray scattering study*
C. REVENANT, G. RENAUD, R. LAZZARI AND J. JUPILLE,
Phys. Rev. **B 79**, 235424 (2009)

[3.4] (11) *Adhesion of growing nanoparticles at a glance: Surface differential reflectivity spectroscopy and grazing incidence small angle x-ray scattering*
R. LAZZARI, G. RENAUD, C. REVENANT, J. JUPILLE AND Y. BORENSZTEIN,
Phys. Rev. **B 79**, 125428 (2009)

[2.7] (2) *Prebonding Thermal Treatment in Direct Si-Si Hydrophilic Wafer Bonding*
C. Ventosa, F. Rieutord, L. Libralesso, F. Fournel, C. Morales, H. Moriceau
J. Electrochem. Soc. **156** (11) H818 (2009)

[2.2] (4) *Hydrated cholesterol: Phospholipid domains probed by synchrotron radiation*
Solomonov I, Daillant J, Fragneto G, Kjaer K, Micha J.S., Rieutord F, Leiserowitz L
Euro. Phys. J. **E 30** p 215 (2009)

[2.2] (8) *Elastic relaxation in patterned and implanted strained silicon on insulator*

S. Baudot, F. Andrieu, F. Rieutord, J. Eymery
J. Appl. Phys. **105** (11) 114302 (2009)

[2.2] (1) *Mechanism of Thermal Silicon Oxide Direct Wafer Bonding*
C. Ventosa, C. Morales, L. Libralesso, F. Fournel, A.M. Papon, D. Lafond, H. Moriceau, J.D. Penot, F. Rieutord
Electrochem. Solid State Lett. **12** (10) H373 (2009)

[0.9] (3) *Structural properties of Ge/Si(001) nano-islands by diffraction anomalous fine structure and multiwavelength anomalous diffraction*
M.-I. RICHARD, N.A. KATCH, M.G. PROIETTI, H. RENEVIER, V. FAVRE-NICOLIN, Z. ZHONG, G. CHEN, M. STOFFEL, O. Schmidt, G. Renaud, T.U. Schülli and G. Bauer
Eur. Phys. J. Special Topics **167**, 3 (2009)

[0.9] (4) *Real-time icosahedral to fcc structure transition during CoPt nanoparticles formation*
Penuelas J, Andreaaza P, Andreazza-Vignolle C, Mottet C, De Santis M and Tolentino HCN
Eur. Phys. J. Special Topics **167** p19-25, (2009)

[0.5] *Structure, morphology and magnetism of an ultra-thin [NiO/CoO]/PtCo bilayer with perpendicular exchange bias*
H. C. N. Tolentino, M. De Santis, J.-M. Tonnerre, A. Y. Ramos, V. Langlais, S. Grenier, A. Bailly
Brazilian Journal of Physics **39** p150 (2009)

« Towards synchrotron-based nanocharacterization »
P. Bleuet, L. Arnaud, X. Biquard, P. Cloetens, L. Doyen, P. Gergaud, P. Lamontagne, M. Lavayssière, J.-S. Micha, O. Renault, F. Rieutord, J. Susini, O. Ulrich
AIP Conf. Proc. **1173** 181 (2009)